Monocyte-macrophage spatial dynamics promote pre-crown-like niches in early obesity

Cooper Stansbury, Gabrielle A. Dotson, Indika Rajapakse, Alnawaz Rehemtulla, Lindsey A. Muir

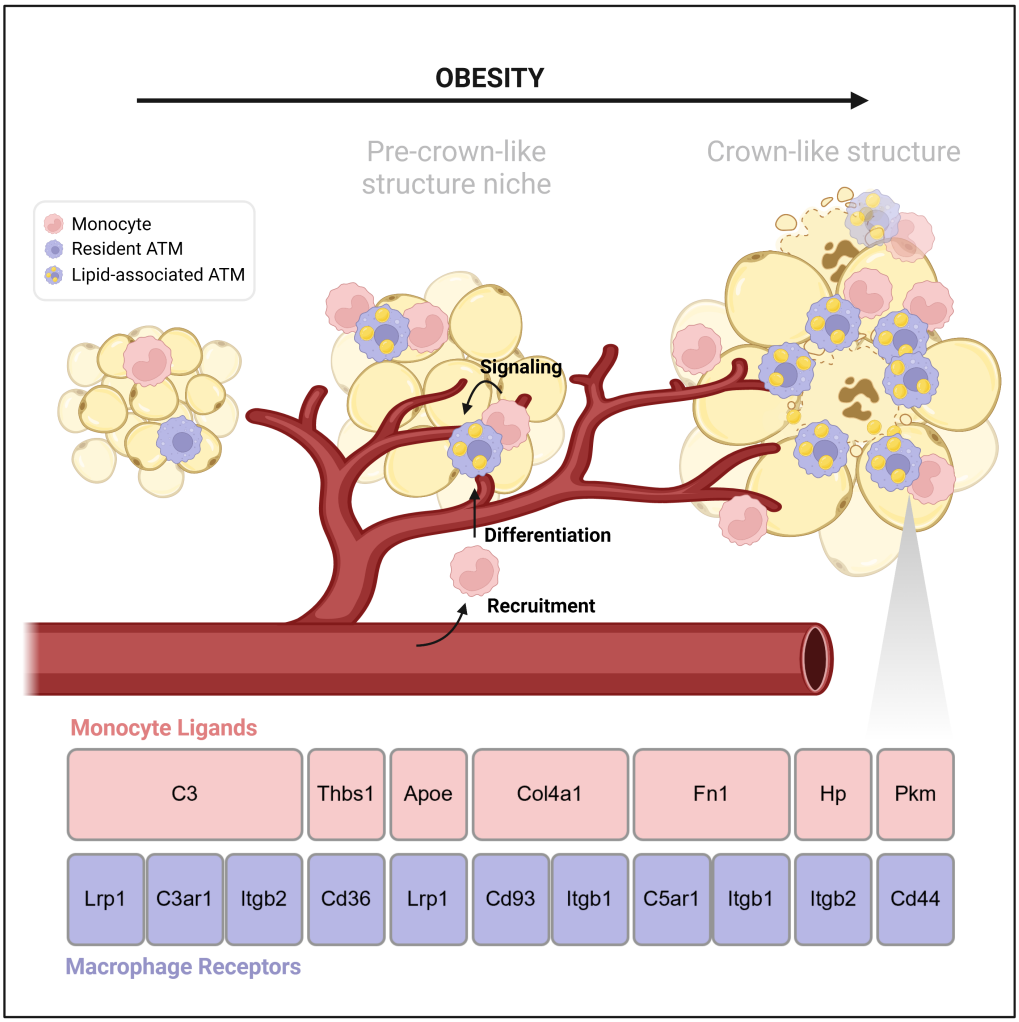

Highlights:

- Spatial transcriptomics shows innate immune cell dominance in obese adipose tissue
- Increased monocyte signaling accompanies infiltration in obesity
- Pre-crown-like niches precede crown-like structure formation
- Influential monocyte-macrophage ligand-receptor pairs emerge at crown-like niches

Monocyte-macrophage spatial dynamics promote pre-crown-like niches in early obesity

Cooper Stansbury[1,†], Gabrielle A. Dotson[1,†], Indika Rajapakse[1,2], Alnawaz Rehemtulla[2], and Lindsey A. Muir[1*]

[†]These authors contributed equally to this work.

[1]Department of Computational Medicine and Bioinformatics, University of Michigan, Ann Arbor, MI 48109 USA
[2]Department of Mathematics, University of Michigan, Ann Arbor, MI 48109 USA
[3]Department of Hematology/Oncology, University of Michigan, Ann Arbor, MI
[*]To whom correspondence should be addressed (lindmuir@umich.edu; 1600 Huron Parkway, NCRC B520-3368, Ann Arbor, MI 48109).

Abstract

Objective: Obesity drives significant changes in adipose tissue that precede development of tissue and systemic insulin resistance. Immune cell infiltration and inflammation are known contributors to these changes but there is limited understanding of their spatial context tissue-wide. We sought to identify spatial patterning in epididymal adipose tissue immune cells in a time course of diet-induced obesity in mice.

Methods: Using spatial transcriptomics and single-cell RNA-sequencing, we identified dominant cell type signatures preserved in their anatomical context, quantified gene expression patterns at spots throughout adipose tissue, performed cell type network analysis, and investigated ligand-receptor colocalization.

Results: Our data support increased innate immune cells, including macrophages, monocytes, and innate lymphoid cells with tissue-wide interspersion, and dampened adaptive immune cell signatures with obesity. Network analysis identified increased heterogeneity in all major immune cell types, consistent with increased subtypes. To capture tissue dynamics at obesity onset, we draw on mathematical principles from linear algebra and spectral graph theory and provide a framework for better understanding cell cooperation toward emergence of multicellular tissue function. Ligand receptor analysis in spatial transcriptomics data at 8 and 14 weeks of high fat diet feeding shows colocalization of monocyte-macrophage ligand receptor expression consistent with increased crosstalk in obesity. Furthermore, we identify in spatial data crown-like structure neighborhoods and pre-crown-like niches, which are enriched in ligand receptor pairs that suggest monocyte-driven signaling to macrophages in early obesity.

Conclusion: The culmination of these analyses revealed a widespread paradigm shift in ligand-receptor activity with near-exclusive macrophage-macrophage or monocyte-macrophage interactions at crown-like structures across adipose tissue in early obesity.

Keywords: Obesity, crown-like structures, spatial transcriptomics, single cell RNA-sequencing, immune cells, adipose tissue

1 Introduction

The global increase in obesity raises significant concern about the development of cardiovascular and metabolic disease, increased risk of adverse events in viral infection, and economic and health care costs [1, 2]. Changes in white adipose tissue (WAT) immune cell types and polarization occur in obesity and are associated with metabolic dysfunction in mice and humans [3, 4, 5, 6].

Population and single-cell transcriptomics enable low-bias characterization of these obesity-related changes in WAT immune cells [7, 8, 6]. However, the molecular events triggering tissue dysfunction remain poorly understood in their anatomical context, which is lost with tissue digestion. Tissue immunostaining captures anatomical context but is limited to a small number of concurrent markers that may not fully distinguish cells with similar surface proteins. In adipose tissue, macrophages (ATMs) and dendritic cells (ATDCs) have been challenging to distinguish, yet have unique participation in tissue homeostasis and development of insulin resistance [9, 10, 11]. Thus low-bias capture of immune cells and subtypes within a tissue landscape will be critical for identifying functional distinctions relevant to disease.

Spatial transcriptomics (ST) captures signatures of gene expression across tissue sections, which in studies of amyotrophic lateral sclerosis (ALS) led to discovery of new anatomical subregions and spatiotemporal patterns underlying tissue dysfunction [12, 13, 14, 15, 16]. ST was recently used to profile different adipocyte subtypes with distinct responses to insulin stimulation in human adipose tissue [17]. Here, we mapped murine adipose tissue and immune cell populations in obesity using a combination of spatial transcriptomics and single cell RNA-sequencing. Over a time course of diet-induced obesity and development of the pre-diabetic state, one of our primary goals was to capture dynamics of early immune cell infiltration as tissue dysfunction appears. We present the tissue landscape as a network of cells and interrogate spatial patterning and cell-cell communication in early obesity. Our analyses capture early monocyte infiltration, progressive dominance of monocyte and macrophage crosstalk, and dampening of adaptive immune cell signatures. Furthermore, ligand-receptor analyses show putative monocyte-macrophage interactions in pre-crown-like anatomical neighborhoods by 8 weeks of high-fat diet feeding, implicating monocyte signaling in development of crown-like structures in a role distinct from their differentiation into ATMs.

2 Results

2.1 Spatial analysis of adipose tissue across early obesity

We evaluated tissue and metabolic function in our diet-induced obesity model using mice fed a normal diet (ND), a high-fat diet for 8 weeks (8w), and a high-fat diet for 14 weeks (14w) (Figure 1A). As expected, mice fed a high-fat diet (HFD) gained body and epididymal white adipose tissue (eWAT) weight (Figure 1B-D). Glucose tolerance tests (GTT) showed increased area under the curve (AUC) starting at one week of HFD feeding, with the highest AUC and variability at intermediate time points (Figure 1E,F). Adipocyte sizing showed increased frequency of large adipocytes and greater mean adipocyte size in the 8w and 14w cohorts (Figure 1G,H). These data are consistent with pre-diabetes of this HFD-fed model, showing early insulin resistance during HFD feeding and a period of variable insulin resistance that aligns with dynamic restructuring of adipose tissue.

Changes in SVCs in murine diet-induced obesity include immune cell infiltration and activation that progressively disrupts homeostatic mechanisms [18, 5, 11, 19]. To capture this changing tissue landscape, we performed spatiotemporal molecular profiling, which can uncover key patterns in breakdown of tissue function [13, 14]. Here, we spatially profiled genome-wide transcripts across eWAT sections from ND and HFD-fed mice using the Visium (10X Genomics) spatial transcriptomics (ST) platform [20, 17]. We initially evaluated expected immune cell and obesity-related gene expression, and found increased pan-immune cell *Ptprc* (*CD45*), myeloid-associated *CD68*, recruited ATM marker *Itgax* (*CD11c*), resident ATM marker *Mrc1*, and *Trem2*, which is expressed in lipid-associated ATMs and has proposed functions in protective lipid homeostasis [7, 21, 22] (Figure 1I,J). *Adipoq* progressively decreased as expected in the HFD-fed conditions.

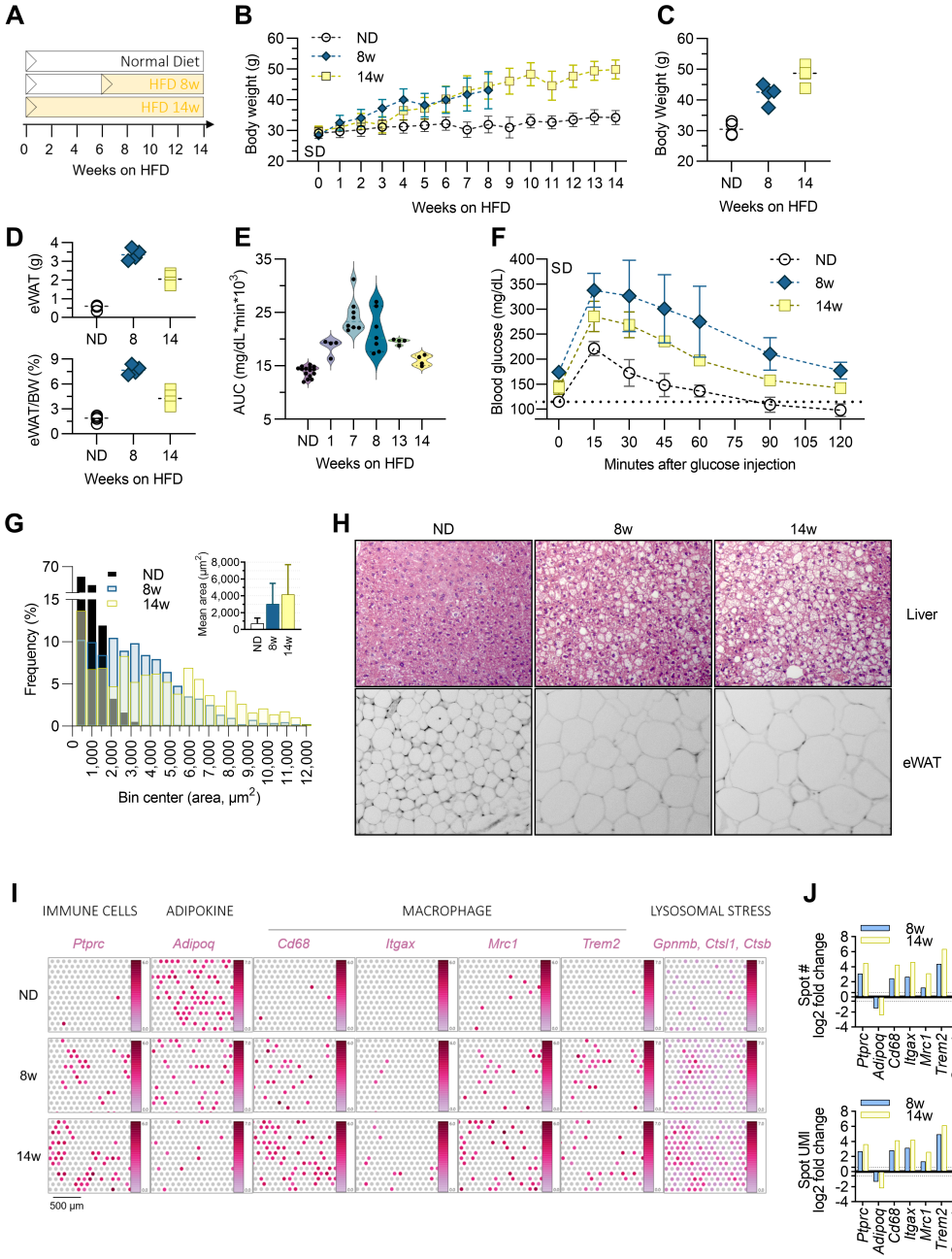

Figure 1: **Diet-induced obesity and adipose tissue remodeling. (A)** Time course for mice fed a 60% high-fat diet (HFD) for 8 weeks (8w) or 14 weeks (14w), versus normal diet (ND) controls. Measurements included weight gain **(B)**, final body weight **(C)**, epididymal adipose tissue (eWAT) weight and eWAT as a percentage of body weight **(D)**, and glucose tolerance test data showing area under the curve (AUC) across time points **(E)** and glucose measurements for cohorts one week prior to endpoint tissue collection **(F)**. **(G)** Frequency distribution and average adipocyte size in eWAT of ND, 8w, and 14w cohorts. **(H)** Representative images from H&E staining of eWAT and liver. **(I)** Representative maps showing spatially preserved gene expression in eWAT. Each spot is a 55 μm diameter transcript capture area from a tissue section, colored corresponding to the expression level ($\log_2$-transformed) of select obesity-related genes. **(J)** Gene expression changes in HFD-fed mice compared to ND mice corresponding to the genes shown in part (I). Upper graph, $\log_2$(fold change) in the quantity of spots in HFD cohorts; Lower graph, $\log_2$(fold change) in average tissue-wide expression of a gene in HFD cohorts.

2.2 Breakdown of adipose tissue immune cell networks in early obesity

Multiple nuclei can contribute transcripts to each spatial data spot, therefore in parallel we performed single-cell RNA-sequencing (scRNA-seq) in SVCs to clarify changes in immune cell types and facilitate signature identification in spatial data. SVCs were isolated from fat pads contralateral to the fat pads used for spatial data and enriched for $CD45^+$ immune cells. We identified cell types in scRNA-seq data using spectral clustering and analysis of signature genes for each cluster, considering expression and uniqueness (Algorithm 1, Table S1, Methods and Materials). Cell type signatures were further verified by alignment with ImmGen profiles (Figure S1). To identify cell types present at spots, we integrated scRNA-seq and ST datasets, determining overlap between a cell type signature and tissue spot gene expression (Figure 2, Algorithm 2, Methods and Materials).

Spectral clustering and data-guided cell type identification yielded six broad immune cell types: monocytes, T cells, ATMs, ATDCs, natural killer cells (NKCs), and B cells (Figure 3A, Figure S1). Changes in the cellular composition of adipose tissue in lean versus obese mice were largely driven by T cells, B cells, and ATMs, where the proportion of single cells classified as T cell and B cell decreased with obesity (17% to 5% in T cells and 22% to 3% in B cells), while the proportion classified as ATMs sharply increased (43% to 76%). These findings are consistent with prior scRNA-seq studies of immune cell populations in diet-controlled mouse models [7, 23], where the same panel of immune cells has been observed and where monocytes and ATMs have been the predominant populations present.

We next established cell type localization patterns in lean and obese adipose tissue. Cell types were assigned to tissue spots hierarchically based on the proportion of their signature expressed at the spot. In this way, the dominant cell type at a spot is the one with the highest number of its representative genes expressed. Dominant cell types across all spots make up the dominant layer, or Layer 1. Layer 2 is assigned as the cell type with the second highest number of signature genes expressed, and the remaining cell types are assigned subsequent layers in the same manner. The outcome of this assignment is a series of layers representing a decreasing likelihood of a given cell type's presence at a particular spot (Figure S2). We refer to this process as spot deconvolution and the resulting tissue assignment layers as 'deconvoluted layers' (Algorithm 2, Figure 2, Methods and Materials). Cell type localization in the dominant layer over time was consistent with trends in cellular composition from the scRNA-seq data, suggesting decreasing T cells and B cells and increasing ATMs in the HFD settings (Figure 3B).

2.3 Spatial network patterning highlights activation of innate and dampening of adaptive immune cell signatures

Inflammation is a key factor in development of adipose tissue dysfunction and insulin resistance in obesity. Cells of the adaptive and innate immune system both contribute to inflammatory processes in adipose tissue, including T cells, B cells, ATMs, ATDCs, and innate lymphoid cells (ILCs) [24]. This network of cells, and their subtypes, modulate inflammation through cytokine and chemokine secretion and cell-cell interactions, reducing anti-inflammatory signaling and promoting proinflammatory cell types and processes over time. To broadly compare patterns of adaptive and innate immune cell networks in obesity, each tissue spot in the spatial data was classed as adaptive (T cell, B cell), innate (monocyte, NKCs, ATM, or ATDC), or mixed type based on the first two tissue assignment layers from Algorithm 2. We found that spots containing only adaptive immune cells consistently decreased with obesity, from 21% to 6% (3.5 fold change), while spots containing only innate immune cells increased with obesity, from 1% to 9% (9 fold change) by 14w (Figure 3C), consistent with known shifts in cellularity with HFD feeding [5]. Among total spots, 75%-85% had mixed type signatures, with the higher frequencies found in obesity. Overall, these data suggest a stronger influence of adipose tissue innate immune cells than adaptive immune cells with obesity, through increased quantity and frequency, strong spatial interspersion, and increased potential for cross-talk with the adaptive immune system (Figure 3C).

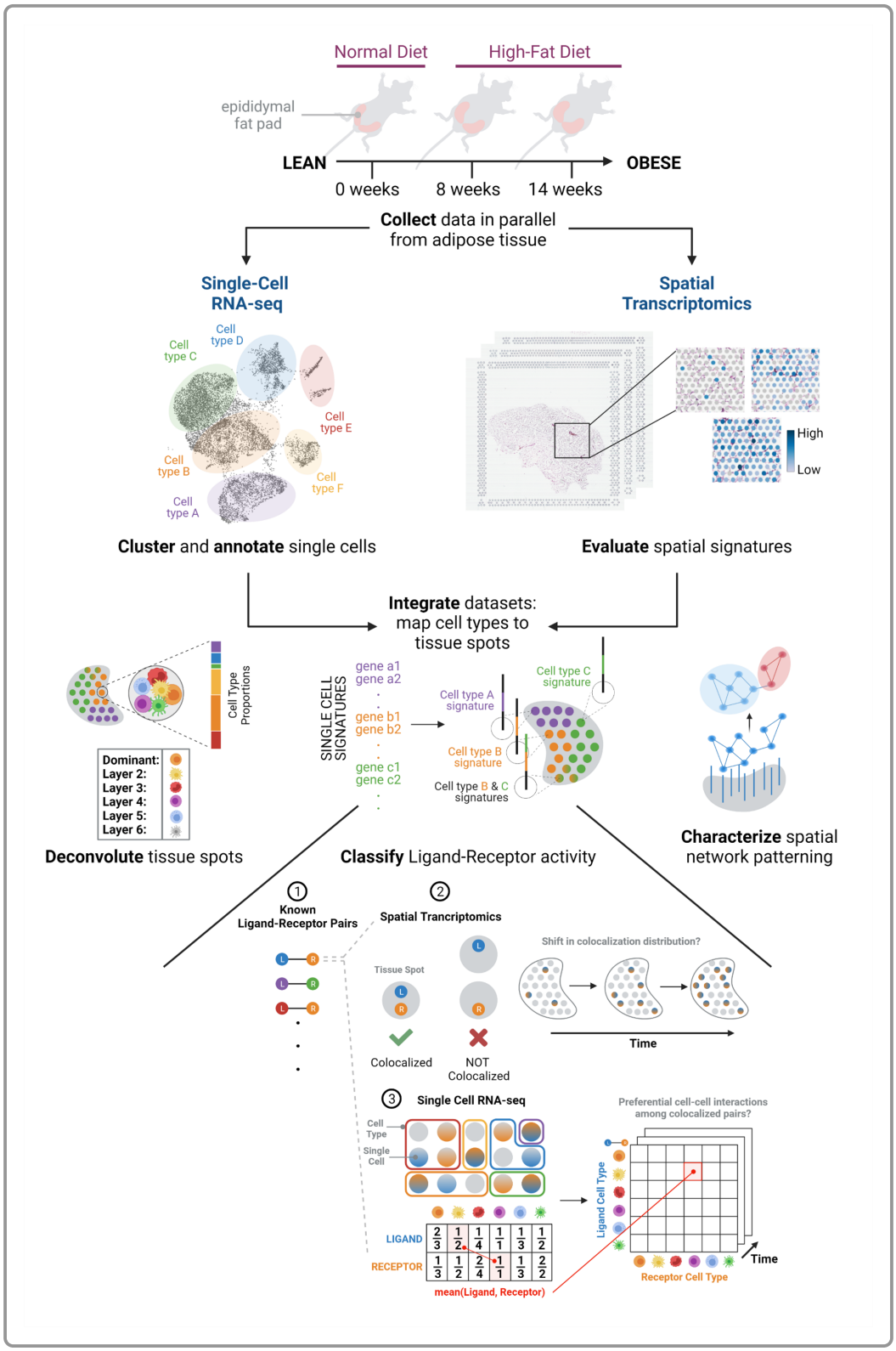

Figure 2: **Workflow of spatial transcriptomics (ST) and single-cell RNA-sequencing (scRNA-seq) data analyses.** Epididymal white adipose tissue was collected from mice in a time course of high fat diet feeding. scRNA-seq data were obtained from within-cohort pooled samples, and ST data were collected from a section of fresh frozen adipose tissue from each diet condition. scRNA-seq data were then pooled across diet conditions, clustered (Algorithm 1), and cell populations were annotated using a data-driven approach (see Methods).

Figure 2: Existing literature and databases were used to query highly-scored markers and call cell types for each cluster. ST data were evaluated for distribution of obesity marker genes. scRNA-seq and ST datasets were integrated by mapping cell types to the adipose tissue sections, performed by finding the overlap between identified cell type signatures (scRNA-seq) and tissue spot expression profiles (ST). Given the size of each tissue spot, more than one cell type signature was likely to be found at each spot. Consequently, every cell type was assigned at each tissue spot based on the proportion of its signature expressed at the spot, generating layers of tissue spot assignments with decreasing likelihood, a process we refer to as spot deconvolution (Algorithm 2). Once tissue spots were annotated, patterns in the intra-cell type spatial tissue network were characterized. Finally, ligand-receptor signaling was classified and colocalization and cell-cell interaction trends characterized (Algorithm 3).

2.4 Turing-inspired analysis reveals increased interconnectivity among monocytes and macrophages

To further assess how immune cells contribute to shifting multicellular tissue function, we described intra- and inter-cell type relationships at the cellular level and identified transcriptional diversity within cell type populations at the genome level. For modeling this tissue morphogenesis, we introduce the notion of the Turing system. Briefly, the Turing system considers the coordinated effect that between-cell and within-cell dynamics have on emerging tissue function (Supplementary Notes)[25]. Here, we characterized between-cell dynamics in terms of correlation between position-specific gene expression profiles weighted by Euclidean distance from ST data and within-cell dynamics in terms of correlation between single-cell gene expression profiles from scRNA-seq data (Methods and Materials). We then captured emerging tissue function in terms of individual cell type contributions, by computing the trade-off between cell and genome connectivity for each immune cell type, derived from between-cell and within-cell dynamics, respectively (Figure S3, Methods and Materials). Our results were consistent with increased contributions from macrophage and monocytes to the changing adipose tissue landscape in obesity (Figure 3D). The individual contributions of T cells and B cells to emerging tissue function decreased with obesity, consistent with localization trends described in Figure 3B.

To determine the contribution of pairs of cell types to tissue function in a potentially coordinated manner – emergence of *multicellular* tissue function – we normalized the emergence of local tissue function (cell and genome connectivity trade-off derived from merged data across *two* cell types) by the emergence of global tissue function (cell and genome connectivity trade-off derived from merged data across *all* cell types). While the majority of cell type inter-connectivities demonstrated decreased or stable coupling with obesity (Figure S4), the inter-cell type contributions between monocyte-macrophage and monocyte-dendritic cell increased in obesity (Figure 3D). In addition, macrophage inter-connectivities were high overall, particularly with other innate immune cell types (Figure S4), while the B-T cell axis had one of the lowest inter-cell type connectivities, decreasing over time (Figure 3D).

The increased monocyte-macrophage and monocyte-dendritic cell inter-cell type relationships in HFD feeding may reflect signatures related to monocyte differentiation [26] or crosstalk between these cells. We further explored the distribution of key myeloid cell markers, and found growing colocalization of common monocyte (*Traf1*, *Ccr2*, *Il1b*, *Napsa*, *Plac8*, *S100a9*, *Msrb1*, *Ifitm6*, *Ms4a4c*, *Cd209a*) and macrophage (*Adgre1*, *Ctsk*, *Lyve1*, *Cd209f*, *Mertk*, *Ccl8*, *Trem2*, *Cd63*, *Mmp12*, *Gpnmb*, *Rhoc*, *Ctsd*, *Mfge8*) markers across the tissue (Figure 3E), indicating a potential role for undifferentiated monocytes in cooperation with macrophages in obesity. In contrast, little to no overlap between B cell and T cell marker colocalization was found 3E), consistent with the low and decreasing B cell-T cell inter-connectivity with obesity.

We next evaluated transcriptional correlation between monocytes and macrophages grew over time as an indicator of a lineage relationship. The correlation between monocyte and macrophage expression profiles increased non-randomly from $R = 0.25$ to $R = 0.30$ ($p < 0.01$) (Figure 3F). While this supports monocyte to macrophage differentiation, the magnitude of the correlation was low, potentially due to increased diversity of subtypes in these populations. Overall, these data support the presence of monocyte-macrophage crosstalk as well as ongoing differentiation of monocytes.

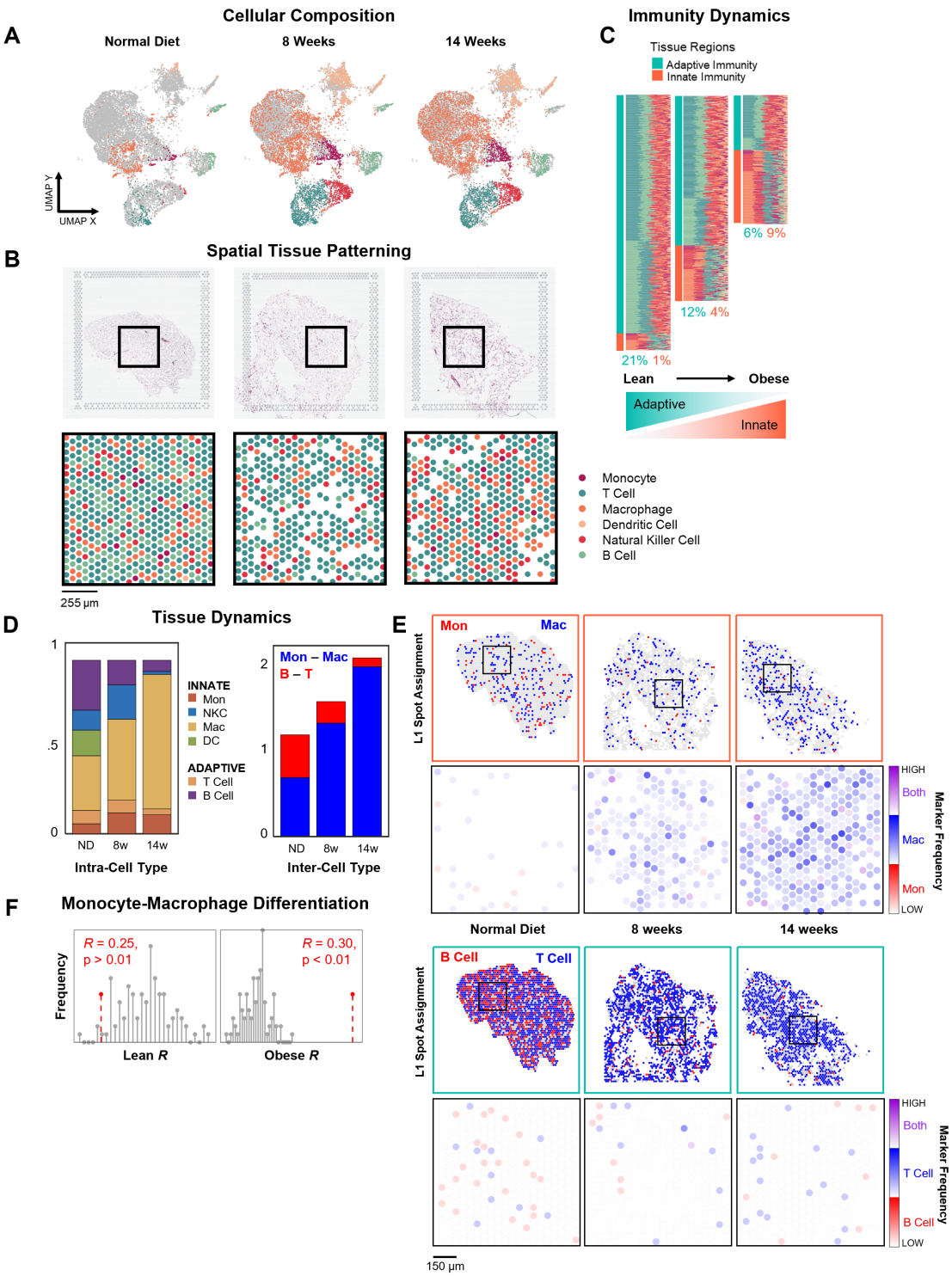

Figure 3: **Immune cell type identification and localization in adipose tissue. (A)** Cellular composition. UMAP projections of scRNA-seq data over time, stratified by cell type. Gray points represent the UMAP projection from pooled clustering of all three samples and colored points represent sample-specific single cells. **(B)** Spatial tissue patterning. (Top) H&E staining of adipose tissue sections. (Bottom) Zoomed view of annotated ST-derived tissue landscapes. Cell type assignments represent the dominant spot assignments after performing spot deconvolution (Algorithm 2). White spaces with no spots indicate non-viable areas of the tissue where there were visible holes and therefore no detectable mRNA levels.

Figure 3: **(C)** Immunity dynamics. Stacked bar plots representing cell type proportions at tissue spots assigned to adaptive or innate immune cell types at each timepoint (denoted by orange and teal vertical bars to the left of the plots). Tissue spots were classified as contributing to adaptive immunity if adaptive cell types colocalized at the spot, meaning deconvoluted tissue assignment layers 1 and 2 (L1 and L2) were assigned as T cell or B cell for those spots. Tissue spots were classified as contributing to innate immunity if innate cell types colocalized at the spot, meaning L1 and L2 were assigned as ATM, monocyte, NKC, or ATDC. Remaining tissue spots were classified as ambiguous tissue regions where L1 was assigned an adaptive cell type and L2 an innate cell type, or vice versa, and are not shown in the figure. Each stacked bar represents a single tissue spot. The height of each component in a stacked bar reflects cell type proportions (the number of genes expressed out of each 50-gene cell type-specific signature). Below plots is a model of the observed adaptive and innate immunity trade-off during obesity progression. We propose that obesity weakens the adaptive immune system and innate immunity concurrently compensates for that weakened immune response over time. **(D)** Tissue dynamics. (Left) Individual cell type contributions to tissue function (normalized to sum to 1). Intra-cell type interactions are quantified by computing the trade-off between cell and genome connectivity for each cell type. (Right) Prominent inter-cell type relationships. Inter-cell type interactions are quantified by dividing the trade-off between cell and genome connectivity for two cell types by the the trade-off between cell and genome connectivity for all cell types (Supplementary Figure 3). **(E)** Inter-cell type spatial distribution. (Boxed in orange) Monocyte (red) and macrophage (blue) spot assignments in the dominant tissue assignment layer. Directly below each plot is a sample region of the tissue showing where monocyte- and macrophage-specific markers localize. A high color intensity indicates a high proportion of monocyte or macrophage-specific markers at the spot. Purple colored regions indicate spots where both monocyte and macrophage markers were found and represent inter-cell type interaction. (Boxed in teal) B cell (red) and T cell (blue) spot assignments in the dominant tissue assignment layer. Directly below each plot is a sample region of the tissue showing where B cell and T cell-specific markers localize. A high color intensity indicates a high proportion of B cell or T cell-specific markers at the spot. Purple colored regions indicate spots where both B cell and T cell markers were found and represent inter-cell type interaction. **(F)** Monocyte-Macrophage differentiation. Stem plot of Spearman correlation (R) between monocyte and macrophage single-cell gene expression profiles in lean versus obese mice. Red stems are the real observed Spearman correlation coefficients in normal diet (left) and high-fat diet (right) mice. Gray stems are the background distribution of Spearman correlation coefficients between randomly-selected single-cell gene expression profiles.

2.5 Increased heterogeneity of signatures within immune cells captures phenotype shifts across adipose tissue

Obesity promotes shifts in immune cell polarization and the appearance of subtypes that affect tissue function. In mice, proportional increases in ATMs relative to tissue weight and patterns of proliferation and apoptosis during weight gain and loss suggest active mechanisms of homeostatic signaling [5] that may eventually be overridden by chronic obesity [27]. We hypothesized that evaluation of immune cell networks in our time course data would provide insight into phenotype shifts that disrupt adipose tissue function.

To better quantify these shifts, we constructed spatial cell networks for each major cell type, where nodes were the tissue spots assigned to the cell type based on the dominant layer and edges between nodes represented a correlation based on transcriptional signature. Surprisingly, cell type network edges decreased universally in obesity, indicating loss of transcriptional correlation among cells of the same type (Figure 4A). This was concurrent with increased heterogeneity in expression of cell type-specific signature genes. Loss of spatial patterning and increased heterogeneity support the emergence of immune cell subtypes in obesity that are not present in the lean state. Macrophages in particular show many phenotypic states [28, 29, 9]. Upon clustering macrophage-classified single cells into two sub-clusters, only one of the two clusters was represented in the normal diet setting while both were represented in the two high-fat diet settings (Figure S5). The emergent cluster in the HFD settings was significantly enriched in *Cd9* ($\log_2$FC of 11.8), which has previously been observed in lipid-laden macrophages in obesity [30, 7, 31]. In contrast to the observed macrophage subpopulations, T cell, B cell, and NKC sub-clusters were less distinct with fewer differentially expressed genes.

2.6 Monocyte and macrophage ligand-receptor pairs dominantly colocalize in obese adipose tissue

To better understand specific interactions that might mediate shifted spatial patterning in obesity, we evaluated colocalized expression of paired ligands and receptors over time. We first captured ligand and receptor expression in adaptive and innate classes, characterizing four interaction states: (1) adaptive ligand and adaptive receptor, (2) innate ligand and innate receptor, (3) adaptive ligand and innate receptor, and (4) innate ligand and adaptive receptor (Materials and Methods). For this study, we determined transcript colocalization of known ligand-receptor pairs as a proxy for cell-cell communication given the restricted area of each tissue spot.

We investigated known ligand-receptor (LR) pairs based on literature and observed increased colocalization across the tissue over time, with increased number of colocalized spots and increased LR pairs per spot (Figure 4B). We then sought to identify the source of expression for colocalized LR pairs. To capture broader trends, we initially used adaptive and innate immune cell categories. Using scRNA-seq data, we determined the frequency of cells expressing the ligand among adaptive cells and the frequency among innate cells, and likewise determined the frequency of cells expressing the receptor among adaptive and innate cells. Based on these data, we generated a score for each LR pair to represent a likelihood of an interaction in the four interaction states described above (Materials and Methods). We found that of the four classes, innate-innate LR pairs were the most frequent (43%), followed by adaptive-innate (25%). Furthermore, innate-innate LR pairs nearly doubled in obesity, comprising 88% of the pair assignments at 14w. (Figure 4C). Overall, these data suggest moderate crosstalk within innate immune cells and between innate and adaptive cells in the lean state that is lost in obesity.

We then explored whether similar patterns of crosstalk could be observed in specific cell types, using the same approach as for the innate and adaptive analysis (Algorithm 3, Figure 2). In first evaluating intra- versus inter-cell type crosstalk, we noted strong inter-cell type interactions in the lean state, while intra-cell type interactions became more prominent in obesity. (Figure 4D). A high percentage of LR pairs contained at least one member assigned to macrophages, especially by 14w (Figure 4E). At 14w, the mean interaction score between across LR pairs between macrophage and other cell types was roughly 25% while interactions between cell types not involving macrophage exhibited average scores below 20%. Furthermore, as evidenced by the heatmap of the number of LR pairs in each cell type interaction, macrophage and monocyte interactions progressively increased in the obesity conditions, concurrent with decreased diversity of cell-cell interactions (Figure 4F).

2.7 Pre-crown-like structure neighborhoods appear in early obesity

Crown-like structures (CLS) appear in adipose tissue in chronic obesity, where macrophages accumulate around dead or dying adipocytes (Figure 5A). We used *Itgax* and *Trem2*, which have roles in CLS formation [21, 32], and *Cd9*, used to identify lipid-laden macrophages, to help define CLS-related areas in ST data in obesity. We noted an increase in these CLS spots in HFD feeding, consistent with their typical emergence beyond about 12 weeks of 60% HFD (Figure 5B). Our CLS criteria were not present in lean adipose tissue, though we did find CLS at 8w of HFD feeding. We used *Cd9* alone to identify tissue spots that could serve as a baseline in lean tissue. We then demarcated neighborhoods around each CLS signature-expressing tissue spot to capture expression from nearby cells and explore features that might be involved in CLS dynamics in obesity (Figure 5C, Materials and Methods).

We first determined whether CLS neighborhoods contained differentially expressed genes compared to control neighborhoods. We compared expression pooled across all ND baseline neighborhoods with expression pooled within each individual CLS neighborhood at 14w, finding that 939 genes were uniquely (compared to control neighborhoods, see Materials and Methods) and significantly differentially expressed ($|\log_2 FC| \geq 1.5$, $p < 0.01$). Of those, 24 genes were differentially expressed in at least 20% of CLS neighborhoods (Figure 5D). Moreover, all differentially expressed genes were up-regulated, with *Trem2*, *Cd9*, and *Itgax* among the most frequently occurring DEGs across CLS neighborhoods, as expected. In addition, we found several other genes related to CLS formation, including *Soat1*, *Hk3*, and *Syngr1* [33, 34].

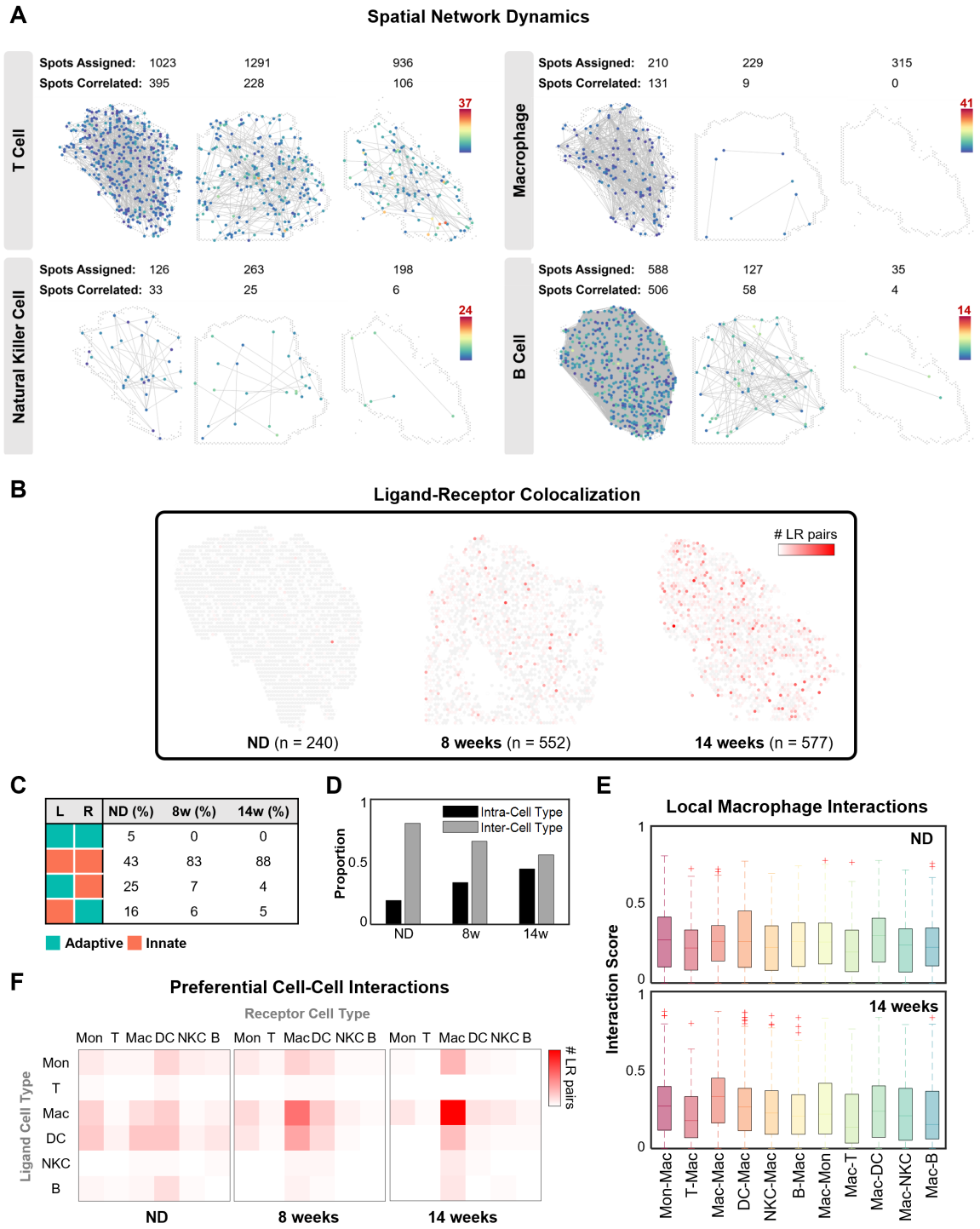

Figure 4: **Intra-cell type spatial patterning. (A)** Network nodes represent transcriptionally correlated tissue spots assigned to the cell type in the dominant tissue assignment layer. Color intensity of network nodes represents the number of cell type-specific signature genes expressed at the spot. The upper bound of the color bar is the maximum number of signature genes (out of 50) expressed at any given spot across all three tissue settings. Network edges represent high correlations (correlation coefficient ≥ 0.85) between cell type-specific gene expression profiles at two spots.

Figure 4: **(B)** Distribution of colocalized ligand-receptor (LR) pairs. Color intensity denotes the number of LR pairs colocalized at the tissue spot (normalized by the total number of tissue spots). **(C)** Percent of LR pairs that preferentially interact between adaptive and/or innate cell types. **(D)** Proportion of ligand-receptor interactions between single cells of the same cell type (intra-cell type) versus single cells of different cell types (inter-cell type) **(E)** Range of interaction scores across all colocalized LR pairs in all macrophage-involved cell-cell pairs. Each LR pair's interaction score between cell types is evaluated by computing the mean between the proportion of single cells of one cell type expressing the ligand and the proportion of single cells of another cell type expressing the receptor. **(F)** Number of LR pairs that preferentially interact between two cell types. Frequencies are normalized by the total number of colocalized LR pairs in the sample. Preferential interaction was determined by evaluating individual LR interaction scores based on the mean proportion of single cells in a cell type expressing the ligand and the mean proportion of single cells in a cell type expressing the receptor (described in Algorithm 3).

We then evaluated how LR colocalization trended with CLS emergence. We found that in addition to increased CLS numbers in obesity, CLS neighborhoods contained an increased number of LR pairs. (Figure 5E). Specifically, LR colocalization at CLS neighborhoods increased from 18% in ND (17% in control neighborhoods) to 58% at 14w (30% in control neighborhoods). These colocalized LRs fell into several categories of expression across the diet conditions, becoming more enriched or depleted across CLSs over time and interacting between different cell types (Materials and Methods). An overwhelming majority of LR pairs demonstrated an overall increase in the proportion of CLS neighborhoods where they colocalized from the lean to obese states (Figure 5F). Most of these were LR pairs that increased from ND to 8w and again from 8w to 14w (54%). Interestingly, there was a considerable proportion (20%) of LR pairs whose involvement at CLS neighborhoods increased from ND to 8w then decreased from 8w to 14w. We previously observed this similar "amplification-attenuation" trend among the intra-cell type tissue contributions where both natural killer cells and monocytes demonstrated increased connectivity within their respective cell type networks followed by weakened connectivity (Figure 3). This trend led us to speculate about a pre-CLS state in our intermediate HFD feeding time point.

To elucidate cell types responsible for driving dynamic signaling at CLS neighborhoods, we revisited cell types found to dominantly express each LR pair from our earlier analysis in Figure 4. Monocytes and dendritic cells dominantly express a large proportion of LR pairs at baseline neighborhoods in the increase-increase group in the ND setting. By 14w, macrophage accounted for the majority of ligands (60.7%) secreted and picked up by receptors (77%) in the CLS niche. We further examined specific LR pairs from the increase-increase group, screening for LR pairs that appeared in CLS neighborhoods only after HFD feeding. We identified 12 LR pairs that colocalized at no baseline neighborhoods in lean adipose tissue then emerged prominently at these sites in obese adipose tissue (Table S2). Of the remaining LR pairs, some involved a ligand and/or receptor with a previously characterized role in obesity, like *C3*, linked to lipid metabolism and contribution to inflammation in adipose tissue during obesity [35]. *C3* was a recurrent, dominantly monocyte-expressed ligand in this group, with an average percent increase in colocalization with receptors at CLS neighborhoods of 54.8% from ND to 14w. *C3* was associated with receptors *Itgax*, *Itgb2*, *C3ar1*, and *Lrp1*, which were expressed by a mix of innate cell types in the data at 8w. At 14w, *C3* only colocalized with receptors associated with macrophages. Similar outcomes were found with analysis of several other LR pairs.

3 Discussion

Inflammation is a prominent feature of obese adipose tissue that contributes to development of insulin resistance. Here, investigation of immune cell signatures in their spatial context highlights the tissue-wide scale of innate and myeloid cell population expansion. While scRNA-seq data improved inference of cell identity, exploring sequencing-based spatial transcriptomic platforms with higher resolution will be valuable [36].

A positive cooperative relationship is consistent with monocyte infiltration and differentiation into macrophages in obesity, and is further supported by the increase in monocyte contribution to tissue function shown in

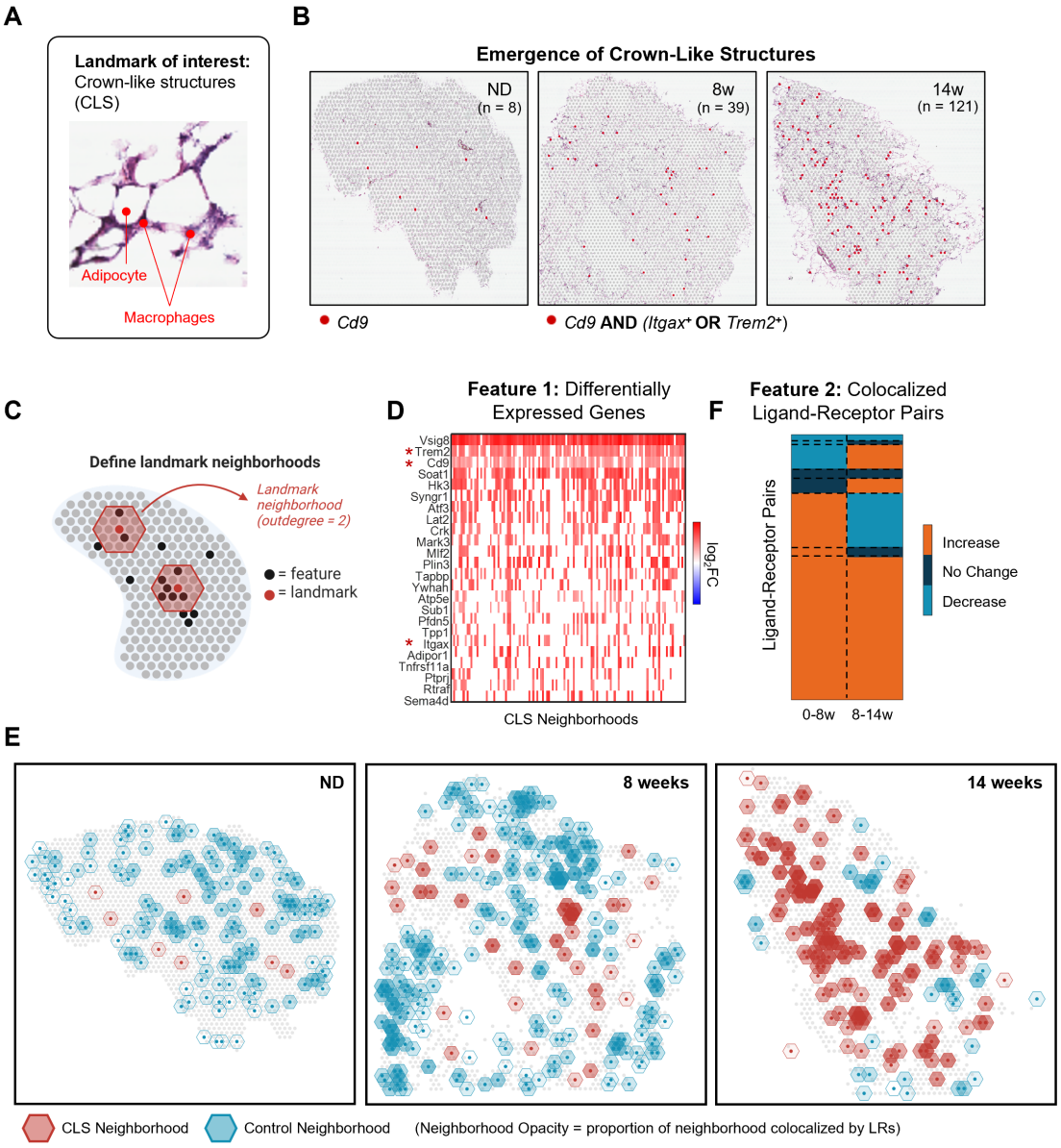

Figure 5: **Emergence of Crown-like Structures (A)** H&E staining of the 14w adipose tissue section showing a characteristic crown-like structure (CLS). **(B)** Identification of CLSs in the ST data. In HFD settings, tissue spots were classified as CLSs if they expressed *Cd9* with either *Itgax* or *Trem2*. As CLSs are not found in lean adipose tissue, only the more general lipid-laden macrophage marker, *Cd9*, was queried in the ND setting. **(C)** Illustration of CLS neighborhood demarcation. Spots within two outdegrees of the CLS-classified spot (landmark) were defined as the CLS neighborhood. Following analyses evaluated different features relative to these neighborhoods. **(D)** Differentially expressed genes ($|\log_2 \mathrm{FC}| \geq 1.5$, $p < 0.01$) found in at least 20% of CLS neighborhoods. Color intensity indicates fold change between ND and 14w. Red values indicate an increase in expression (positive FC) and blue indicates a decrease in expression (negative FC). **(E)** LR pairs in CLS neighborhoods. Red neighborhoods correspond to CLSs while blue neighborhoods correspond to a control population containing housekeeping gene *Ppia*. The transparency of the filled-in neighborhoods indicates the number of colocalized LR pairs found in the neighborhood, with more opaque shading corresponding to a higher number of colocalized pairs. For visual clarity, neighborhoods are shown to an outdegree of 1, but analyses were performed on neighborhoods with an outdegree of 2.

Figure 5: **(F)** Patterns of LR colocalization dynamics at CLS neighborhoods. The majority of LRs increased in colocalization at CLSs from ND to 8w and 8w to 14w (orange-orange block). The second most frequent pattern observed was LRs that increased in colocalization at CLSs from ND to 8w, then decreased from 8w to 14w (orange-light blue block).

Figure 3D. Our spatial patterning analysis showed increased heterogeneity for all immune cell types. This finding is consistent with adoption of additional polarization states or phenotypes in immune cells in obesity, for example in *Cd9*-enriched macrophages in obesity [30, 7, 31]. Emerging subtypes in other immune cells were less identifiable, possibly due to lower potential for different functional states in those cell types. Known shifts in subtypes include increased $Cd8^+$ T effector and $Cd4^+$ T_H1 cells and decreased regulatory T cells in obesity [37, 11, 19]. Additionally, while increased IgG^+ B cells have been observed in obese murine visceral adipose tissue [38], the only differentially expressed gene in our B cell sub-clustering was the immunoglobulin gene, *Ighg3*, which was enriched in the high-fat diet settings ($\log_2$FC of 1).

Ligands and receptors expressed in innate cells preferentially colocalized across the obese tissue compared to ligands and receptors expressed in adaptive cells or a combination of innate and adaptive cells. These interactions were predominantly from monocytes and ATMs, consistent with their increased quantity in obesity. Our adaptation of Turing's system for within-cell and between-cell dynamics similarly captured an increasing contribution of monocytes and ATMs to tissue function in obesity, alongside a decreasing contribution of adaptive immune cells, NK cells, and ATDCs.

In addition, we provide a proof-of-concept analysis for predicting the trajectory of tissue states in disease. Our model of disrupted tissue morphogenesis in disease could be generalized to other tissues to define a disease index that distinguishes healthy from disrupted tissue states predictive of metabolic dysfunction or other diseases. Relevant to obesity are liver and intestinal tissue, which have defined tissue changes in gene expression in obesity [39, 40, 41]. Integrated analysis of spatial and single-cell transcriptomics in these tissues could allow us to establish a consistent inter-tissue index in obesity.

Understanding CLS formation and dynamics in obesity is an important goal, as high CLS content in adipose tissue is linked to more severe clinical outcomes of obesity and higher risk for cancers [42, 43, 44, 45]. Our analyses of differential and ligand-receptor expression at mapped CLSs revealed a shift toward monocyte-driven signaling to lipid-associated ATMs in short-term HFD feeding. Notably, the expression patterns observed in pre-CLS niches at 8w of HFD feeding precede observable CLS architecture. These data support a model in which monocytes, recruited from circulation, both differentiate into lipid-associated macrophages and participate in cell-cell signaling via specific obesity-activated ligands.

Some obesity-related changes in adipose tissue immune cells persist even in weight loss [27], highlighting the need to better understand mechanisms that promote adipose tissue dysfunction. These mechanisms could also tie obesity to the risk for other conditions, including cardiovascular disease and cancer [46, 47], with one study finding that metabolically activated macrophages in mammary adipose tissue promotes triple-negative breast cancer [48]. Future studies using time course spatial transcriptomics could be particularly powerful in understanding tissue dynamics and the evolution of cell-cell communication in adipose tissue.

A limitation of our study is that protein-level markers have not been confirmed to align with these gene expression signatures in our CLS analysis, which would be a useful extension supporting our model. The presence of known CLS-related genes in our data did, however, support our selection method for identifying CLS spots. Additionally, while our data capture the dominant immune cell types at spots with colocalized LR pairs, the potential for multiple nuclei per spot in ST data means that we cannot rule out participation of other immune cells, non-immune SVCs, or adipocytes in the identified interactions. Further investigation of CLS formation and dynamics and immune cell activity in early obesity could help untangle these interactions and uncover mechanisms that contribute to adipose tissue and metabolic dysfunction.

4 Materials and Methods

4.1 Animals

C57BL/6J mice were used for these experiments (Jackson Laboratories 000664). Male mice were fed ad libitum a control normal chow diet (ND; 13.4% fat, 5L0D LabDiet) or high-fat diet (HFD; 60% calories from fat, Research Diets D12492) for the indicated amount of time starting at 9 weeks old. Animals were housed in a specific pathogen-free facility with a 12 h light/12 h dark cycle and given free access to food and water except for withdrawal of food for temporary fasting associated with glucose tolerance tests. All mouse procedures were approved by the Institutional Animal Care and Use Committee (IACUC) at the University of Michigan (Animal Welfare Assurance Number D16-00072 (A3114-01), #PRO00008583), and care was taken to minimize suffering adhering to the Institute of Laboratory Animal Research Guide for the Care and Use of Laboratory Animals.

4.2 Glucose tolerance tests

For glucose tolerance tests (GTT), starting four hours into the light cycle, mice were fasted with ad libitum access to water for six hours in clean cages. A 100 mg/mL D-glucose (Sigma G7021) solution was prepared in sterile -/- DPBS and injected at 0.7 g/kg of body weight. Area under the curve (AUC) calculations were performed using the log trapezoidal method.

4.3 Stromal cell isolation

Stromal vascular cells (SVCs) were collected from adipose tissues as in [5]. After cardiac perfusion, adipose tissues were collected, minced finely to 3-5 mm pieces, and added to ice cold HBSS+Ca/Mg. Up to 1.5 g of tissue per sample was digested in 10 ml of 1 mg/mL collagenase II (Sigma C68850) in HBSS+Ca/Mg at 37°C for 45 minutes with vigorous shaking. Digests were filtered through buffer-soaked 100 micron cell strainers and centrifuged at 300 x g at 4C to pellet SVCs.

4.4 Immune cell enrichment and single-cell RNA-sequencing

SVCs were enriched for $CD45^+$ immune cells using Biolegend MojoSort Mouse CD45 Nanobeads (Biolegend 480027), following the manufacturer's protocol. Briefly, SVC pellets were resuspended in 1 mL MojoSort Buffer, pooling the four samples from each cohort into a single respective cohort tube (ND, 8w, 14w), then filtered through a 70 micron cell strainer and placed in 5 mL polypropylene tubes. After addition of nanobeads, samples were sequentially processed for magnetic separation. To increase purity, three magnetic separations in total were performed on the labeled fractions. Final cell suspensions were filtered through 40 micron pipette tip filters. Cell viability was >80% with <15% aggregation.

4.5 Spatial transcriptomics tissue preparation

Within 30 minutes of cardiac perfusion, adipose tissues were pre-soaked in ice cold O.C.T. Compound (VWR 25608-930) and placed in biopsy cryomolds (VWR 25608-922) with fresh O.C.T., rapidly frozen by immersion in liquid nitrogen-cooled isopentane, and kept on dry ice or at -80°C until sectioning. Fresh tissue sections were cut at 10 μm after 20 minute equilibration in a cryochamber set to -26°C or below with specimen arm at -40°C. Samples were placed on a 10X Genomics/Visium Spatial Gene Expression slide and processed by the University of Michigan Advanced Genomics Core according to the manufacturer's protocol.

4.6 Single-cell RNA-sequencing data processing

Raw single-cell RNA-sequencing data were processed using the 10X Genomics CellRanger (version 4.0.0) pipeline and resulting feature-barcode matrices were loaded into MATLAB for further processing using an in-house pipeline. Single cells (barcodes) with fewer than 500 expressed genes were filtered from the data matrix leaving 1,231 cells in the ND setting, 6,011 cells in the HFD8 setting, and 6,258 cells in the HFD14 setting. Genes (features) were filtered out according to the same criteria used to filter genes in the

spatial transcriptomics data. The median number of genes expressed per cell for each setting was: 1,707, 1,644, and 1583, respectively. Additionally, filtered matrices were normalized in the same way as the spatial transcriptomics data matrices.

4.7 Spatial transcriptomics data processing

Raw sequencing data were processed using the 10X Genomics SpaceRanger (version 1.0.0) pipeline with mouse reference GRCm38, and resulting feature-barcode matrices were loaded into MATLAB for further processing using an in-house pipeline. Matrices contain absolute transcript counts, reported as unique molecular identifier (UMI) counts, pertaining to each feature (rows) and tissue-associated barcode (columns). Informed by the 10X Genomics Loupe Browser visualization of barcoded tissue spots overlaying tissue histology images, we filtered out barcoded spots that overlapped visible holes in the tissue and therefore had no tissue material for gene expression to be detected at. This resulted in no barcoded spots being discarded from from the ND setting, 1,458 being discarded from the HFD8 setting, and 490 from the HFD14 setting. After filtering, there were 2,035 , 1,936, and 1,504 viable spots remaining in each setting, respectively. Genes that were detected at no barcoded tissue spots (indicated by a row sum of 0) were filtered from the feature-barcode matrices. Additionally, we filtered out mitochondrial and ribosomal genes as well as genes known to be linked to mapping errors (*Malat*, *Lars2*, *Kcnq10t1*, and *Gm42418*) [49]. Our working features list contained 19,941 total genes. The median number of expressed genes per tissue spot for each setting was: 91, 105, and 173, respectively. Finally, we normalized each feature-barcode matrix by dividing by a scaling factor - computed as the median UMI counts per barcode divided by the total UMI counts per barcode - then log-transforming the matrix.

4.8 Integration of spatial and single-cell transcriptomics data

The cellular composition of each tissue section was characterized by mapping expression profiles from scRNA-seq data to their paired spatial landscape. To achieve this, we first aggregated our scRNA-seq data matrices, mean-centered and dimensionally reduced the resulting matrix to the first 20 singular vectors, then performed spectral clustering using Euclidean distance as the metric for generating the similarity graph. Informed by known cell types found in adipose tissue from literature, we selected for 15 clusters (k = 15). We then employed a data-guided cell type identification approach where we scored markers for each cluster based on ubiquity (percent of cells in the cluster expressing each gene), cluster-averaged expression (average expression of each gene among all cells in the cluster), and uniqueness (see 'Marker Uniqueness' subsection). For each cluster, the top 50 genes with the highest cumulative score that were also expressed across all three dietary settings and expressed in the spatial transcriptomics data, were selected as cluster-specific signatures. We used prior literature and the CellMarker database [50] to query these signatures and call cell types for each cluster. We further narrowed our set of clusters by removing those indicative of fibroblast contamination, removing those of unknown lineage whose signatures contained non-essential genes, and merging clusters with redundant cell type classifications, leaving us with six total clusters. We validated our cell type annotations using Immgen and found that they aligned with Immgen signatures [51]. To annotate our spatial transcriptomics tissue sections, we mapped cell types identified from the scRNA-seq data to tissue spots, based on the proportion of signature genes expressed at each spot (see 'Spot Deconvolution' subsection).

4.8.1 Marker uniqueness

To evaluate the uniqueness of potential cell type markers to a cluster, we found the ratio of the total number of clusters overexpressing a given gene (fold change ≥ 2) to the number of times that gene is overexpressed by the cluster of interest. The resulting value increases a marker's score proportional to how frequently we see the gene expressed highly in one cluster compared to all other clusters, but offsets the score if the gene is highly expressed in multiple clusters. Ultimately, non-unique genes rank low with this approach. We found that this approach is similar to the Term Frequency-Inverse Document Frequency (TF-IDF) technique commonly applied in machine learning contexts to determine the importance of a word within a document or set of documents [52]. For proof-of-concept, we adapted the TF-IDF technique for marker ranking by treating documents as clusters and words as genes, where term frequency corresponded to the number of

times a given gene is overexpressed by the cluster of interest and inverse document frequency to the number of clusters overexpressing the gene. In doing so, we yielded similar results (data not shown).

4.8.2 Spot deconvolution

Given the thickness of tissue sections and diameter of tissue spots, it is likely that two or more cell identities will colocalize at the same tissue spot. To deconvolute each spot into their possible cellular components, we start by defining a dominant tissue layer wherein a cell type is assigned to a spot if at least five of the cell type-specific signature genes are expressed at the spot and a higher proportion of its signature is expressed at the spot than any other cell type. We define subsequent tissue layers by assigning remaining cell types to each tissue spot following the same criteria as long as the cell type has not already been assigned to the spot in a previous layer. Additionally, we impose a tiebreak condition for when two or more cell types express the same number of genes at a spot. When this happens, the tied cell types are assigned according to highest to lowest cumulative expression of their expressed signature genes. With this approach, each cell type has an equal likelihood of being assigned to a layer, giving us a total number of layers equivalent to the number of cell types identified in the tissue.

4.9 Modeling tissue function

While our spatial transcriptomics data is not single-cell resolution, we are able to assign a dominant cell type to each tissue spot based on the expression of cell type-specific signatures. We can then treat each tissue spot as an individual cell in our model of emerging tissue function. While we also described non-dominant layers of cell type assignments at each spot, we focus our model on the dominant cell type assignment. Our model draws on two subnetworks of the overall tissue network - the cell-cell network and within-cell genome network. Taken together, we can represent each cell type's individual contribution to tissue function and define an index describing the tissue's state in terms of cellular and genome connectivity.

4.9.1 Cellular connectivity

Spatial transcriptomics captures the expression profiles of cells tissue-wide in Euclidean space, allowing us to observe patterns of between-cell connectivity across the tissue. We start by characterizing *intra*-cell type relationships within individual cell populations across the tissue (emergence of tissue function) by finding the transcriptome-wide correlation between tissue spots assigned to a given cell type. We then weight each pairwise correlation coefficient by the Euclidean distance between their corresponding tissue spots, generating an adjacency matrix. We next perform eigenvector decomposition on the normalized Laplacian of the adjacency matrix to obtain the Fiedler number, representing the connectivity of the network of transcriptionally similar cells across the tissue – cell connectivity. The cell type-specific Fiedler number is then divided by the number of tissue spots assigned to the cell type to normalize for the variability in network sizes across the tissue.

To capture *inter*-cell type contributions to tissue function (emergence of *multicellular* tissue function) we consider a network of networks where each cell type is a subnetwork within the larger tissue network. We repeat our previous steps, this time generating an adjacency matrix based on the correlation in expression between tissue spots from two cell types instead of one. We do this for every pair of cell types represented in our tissue samples to demonstrate how cell type coupling contributes to tissue function.

4.9.2 Genome connectivity

From single-cell RNA-seq, we compare the diversity in gene expression profiles within a given cell type to capture within-cell genome connectivity across the tissue. Similar to our computation for cellular connectivity, we find the transcriptome-wide correlation between single cells classified as a given cell type. We then perform eigenvector decomposition on the normalized Laplacian of this correlation matrix to obtain the Fiedler number which we use to define genome connectivity. Again, we normalize the Fiedler number, this time dividing by the number of single cells assigned to the cell type.

4.10 Ligand-receptor analysis

Known ligand-receptor pairs in mice were taken from a compendium of pairs reported throughout the literature compiled by the Lewis Lab at UCSD. [53]. For each ligand-receptor pair and timepoint, we scanned the tissue space to identify tissue spots where both the ligand and receptor of the pair colocalize. We define colocalization as the spatial overlap or co-expression of the ligand and receptor (UMI count > 0) belonging to a known pair at the same x-,y- coordinate (tissue spot) in the spatial transcriptomics data. Paired ligands and receptors that colocalized at at least one tissue spot were further queried for cell-type specific expression at the single-cell level, where the independent expression of the ligand and receptor in adaptive and innate immunity cells was evaluated. The proportions of single cells annotated as: (1) adaptive immunity cell types that expressed the ligand, (2) adaptive immunity cell types expressing the receptor, (3) innate immunity cell types expressing the ligand, and (4) innate immunity cell types expressing the receptor were captured in a 2-by-2 contingency table. The UMI count cutoff for ligand or receptor expression was 3 and pairs where the ligand and/or receptor were not expressed in more than 1% of cells in at least one cell type were discarded. Based on these proportions, we developed an interaction score between the immunity classes for each LR pair where we took the mean of the ligand immunity class proportion and a receptor immunity class proportion, allowing scores to represent the likelihood that the LR pair interacts between those two immune cell classes. We generated local state matrix to reflect these scores, where for a given ligand-receptor pair the intra-interaction between the ligand and receptor in adaptive cells (mean of proportions 1 and 2), the intra-interaction between the ligand and receptor in innate cells (mean of proportions 2 and 3), the inter-interaction between the ligand in adaptive and receptor in innate cells (mean of proportions 1 and 4), and the inter-interaction between the ligand in innate cells and receptor in adaptive cells (mean of proportions 3 and 2) were captured. For each LR pair, we could then determine which class had the highest score, which we interpret as the preferential immunity class pairing exhibiting that LR pair's signaling. Finally, a global state matrix summarizing these intra- and inter-interactions among all colocalized ligand-receptor pairs was derived by taking the element-wise mean across the local state tables. Local and global state matrices were derived for individual cell types as well, as described in Algorithm 3.

4.11 Tissue landmark analysis

The tissue landmark of focus for this study was crown-like structures (CLSs). To identify tissue positions associated with this tissue niche, we queried each barcoded spot for expression of the macrophage marker *Cd9* in addition to either *Itgax* or *Trem2*, two markers known to be highly expressed at CLS sites. This selection criteria was applied to our two HFD settings. CLSs are a hallmark of obesity and are not present in lean adipose tissue, so we screened tissue positions in the ND setting using only *Cd9* for a baseline comparison. CLSs involve multiple cells (a ring of macrophages surrounding an adipocyte) and because adipocytes are expanded in size in obese tissue, activity related to these structures span multiple tissue spots. To capture all relevant signals at and around the CLS positions, we defined landmark neighborhoods, centered around each identified CLS that encompass tissue spots within two outdegrees from the center. We also defined control neighborhoods, centered around spots expressing hallmark gene *Ppia*. Control neighborhoods that overlapped with CLS neighborhoods were removed from analysis. We then assessed features at CLS neighborhoods and used control neighborhoods as a background distribution of tissue spots to gauge the significance of observed trends.

For neighborhood differential expression analysis, expression profiles at spots across all neighborhoods in the ND setting were first pooled together by taking the average expression across spots. Differential expression was performed between pooled expression in ND and each individual CLS neighborhood in the 14w setting, where average expression across spots within a neighborhood were used. The same analysis was performed for ND and 14w control neighborhoods. Genes were assessed for how many CLS neighborhoods they were significantly differentially expressed in ($|\log_2 \mathrm{FC}| \geq 1.5$, $p < 0.01$). Overlaps with DEGs in control neighborhoods were filtered.

We evaluated ligand-receptor (LR) signaling at CLS neighborhoods by evaluating the proportion of neighborhood spots colocalized by an LR pair. Only LR pairs found to be colocalized in all three settings were used in this analysis (132 pairs). We evaluated the same proportion for control neighborhoods and compared the average proportion across both sets of neighborhoods for each setting. We also determined how the colo-

calization of each LR pair at CLS neighborhoods changed over time, relative to the control neighborhoods, grouping LRs based on their pattern of change from ND to 8w and 8w to 14w. For example, LR pairs whose colocalization at CLS neighborhoods (percent of neighborhoods where the LR pair was co-expressed in at least one spot) consistently increased over time were grouped together while those whose colocalization increased from ND to 8w then decreased from 8w to 14w were grouped together. Within each group, LR pairs were then ranked in descending order according to their cumulative change over time and those whose rate of colocalization at CLS neighborhoods were not at least 10% different than at control neighborhoods were further disregarded. Individual LR pairs across groups were further evaluated based on observed trends for biological relevance.

Author contributions

Gabrielle A. Dotson: Methodology, software, formal analysis, data curation, writing and editing the manuscript, visualization; **Indika Rajapakse:** methodology, writing and editing the manuscript, supervision; **Lindsey A. Muir:** conceptualization, methodology, investigation, formal analysis, resources, writing and editing the manuscript, visualization, supervision.

Funding

Research reported in this publication was supported by the University of Michigan NIH NIGMS Bioinformatics Training Grant under Award Number 5T32GM070449-15 and the University of Michigan Genome Science Training Program (GSTP) Fellowship funded by NHGRI under Award Number 5T32HG000040-27 to GAD, the Air Force Office of Scientific Research (AFOSR) award FA9550-18-1-0028 to IR, the National Institute Of Diabetes And Digestive And Kidney Diseases of the National Institutes of Health under Award Numbers K01DK116928 and R03DK129636 to LAM, and the National Cancer Institute of the National Institutes of Health under Award Number P30CA046592 by use of the Rogel Cancer Center Single Cell Resource. The content is solely the responsibility of the authors and does not necessarily represent the official views of the National Institutes of Health.

Acknowledgements

We thank Ingrid Bergin and Pavlina Zafirovska for technical assistance in sectioning and staining tissues, Olivia Koues and the University of Michigan Advanced Genomics Core, Evan Keller and Greg Shelley for assistance with single cell sequencing, Alnawaz Rehemtulla for critical feedback and support of the murine studies, Abigail Riesmeyer and Siva Kumar for technical assistance, Stephen Lindsly and Can Chen for their input on data analysis, and Cooper Stansbury for image analysis. We would also like to acknowledge BioRender.com which was used to generate Figures 2 and 6.

Declarations of interest

The authors report no conflicts of interest in this work.

Data and resource availability

The spatial transcriptomics and single-cell RNA-seq datasets generated in this study have been deposited to the Gene Expression Omnibus (GEO) and can be accessed via accession number GSE198012.

References

[1] Ichiro Misumi, Joshua Starmer, Toru Uchimura, Melinda A. Beck, Terry Magnuson, and Jason K. Whitmire. Obesity expands a distinct population of t cells in adipose tissue and increases vulnerability to infection. Cell Reports, 27(2):514–524.e5, 2019.

[2] Haijiang Dai, Tariq A. Alsalhe, Nasr Chalghaf, Matteo Riccò, Nicola Luigi Bragazzi, and Jianhong Wu. The global burden of disease attributable to high body mass index in 195 countries and territories, 1990–2017: An analysis of the global burden of disease study. PLOS Medicine, 17(7):1–19, 07 2020.

[3] Carey N Lumeng, Stephanie M DeYoung, Jennifer L Bodzin, and Alan R Saltiel. Increased inflammatory properties of adipose tissue macrophages recruited during diet-induced obesity. Diabetes, 56(1):16–23, 2007.

[4] Carey N Lumeng, Jennifer B DelProposto, Daniel J Westcott, and Alan R Saltiel. Phenotypic switching of adipose tissue macrophages with obesity is generated by spatiotemporal differences in macrophage subtypes. Diabetes, 57(12):3239–3246, 2008.

[5] Lindsey A Muir, Samadhi Kiridena, Cameron Griffin, Jennifer B DelProposto, Lynn Geletka, Gabriel Martinez-Santibañez, Brian F Zamarron, Hannah Lucas, Kanakadurga Singer, Robert W O'Rourke, et al. Frontline science: Rapid adipose tissue expansion triggers unique proliferation and lipid accumulation profiles in adipose tissue macrophages. Journal of leukocyte biology, 103(4):615–628, 2018.

[6] Lindsey A Muir, Kae Won Cho, Lynn M Geletka, Nicki A Baker, Carmen G Flesher, Anne P Ehlers, Niko Kaciroti, Stephen Lindsly, Scott Ronquist, Indika Rajapakse, et al. Human cd206+ macrophages associate with diabetes and adipose tissue lymphoid clusters. JCI insight, 2022.

[7] Diego Adhemar Jaitin, Lorenz Adlung, Christoph A Thaiss, Assaf Weiner, Baoguo Li, Hélène Descamps, Patrick Lundgren, Camille Bleriot, Zhaoyuan Liu, Aleksandra Deczkowska, et al. Lipid-associated macrophages control metabolic homeostasis in a trem2-dependent manner. Cell, 178(3):686–698, 2019.

[8] Jinchu Vijay, Marie-Frédérique Gauthier, Rebecca L Biswell, Daniel A Louiselle, Jeffrey J Johnston, Warren A Cheung, Bradley Belden, Albena Pramatarova, Laurent Biertho, Margaret Gibson, et al. Single-cell analysis of human adipose tissue identifies depot-and disease-specific cell types. Nature metabolism, 2(1):97–109, 2020.

[9] Lucia Russo and Carey N Lumeng. Properties and functions of adipose tissue macrophages in obesity. Immunology, 155(4):407–417, 2018.

[10] Kae Won Cho, Brian F Zamarron, Lindsey A Muir, Kanakadurga Singer, Cara E Porsche, Jennifer B DelProposto, Lynn Geletka, Kevin A Meyer, Robert W O'Rourke, and Carey N Lumeng. Adipose tissue dendritic cells are independent contributors to obesity-induced inflammation and insulin resistance. The Journal of Immunology, 197(9):3650–3661, 2016.

[11] Cara E Porsche, Jennifer B Delproposto, Elise Patrick, Brian F Zamarron, and Carey N Lumeng. Adipose tissue dendritic cell signals are required to maintain t cell homeostasis and obesity-induced expansion. Molecular and cellular endocrinology, 505:110740, 2020.

[12] Silas Maniatis, Tarmo Äijö, Sanja Vickovic, Catherine Braine, Kristy Kang, Annelie Mollbrink, Delphine Fagegaltier, Žaneta Andrusivová, Sami Saarenpää, Gonzalo Saiz-Castro, Miguel Cuevas, Aaron Watters, Joakim Lundeberg, Richard Bonneau, and Hemali Phatnani. Spatiotemporal dynamics of molecular pathology in amyotrophic lateral sclerosis. Science, 364(6435):89–93, 2019.

[13] Michaela Asp, Stefania Giacomello, Ludvig Larsson, Chenglin Wu, Daniel Fürth, Xiaoyan Qian, Eva Wärdell, Joaquin Custodio, Johan Reimegård, Fredrik Salmén, et al. A spatiotemporal organ-wide gene expression and cell atlas of the developing human heart. Cell, 179(7):1647–1660, 2019.

[14] Wei-Ting Chen, Ashley Lu, Katleen Craessaerts, Benjamin Pavie, Carlo Sala Frigerio, Nikky Corthout, Xiaoyan Qian, Jana Laláková, Malte Kühnemund, Iryna Voytyuk, et al. Spatial transcriptomics and in situ sequencing to study alzheimer's disease. Cell, 182(4):976–991, 2020.

[15] Michael L Wallace, Kee Wui Huang, Daniel Hochbaum, Minsuk Hyun, Gianna Radeljic, and Bernardo L Sabatini. Anatomical and single-cell transcriptional profiling of the murine habenular complex. Elife, 9:e51271, 2020.

[16] Natasja L De Vries, Ahmed Mahfouz, Frits Koning, and Noel FCC De Miranda. Unraveling the complexity of the cancer microenvironment with multidimensional genomic and cytometric technologies. Frontiers in oncology, page 1254, 2020.

[17] Jesper Bäckdahl, Lovisa Franzén, Lucas Massier, Qian Li, Jutta Jalkanen, Hui Gao, Alma Andersson, Nayanika Bhalla, Anders Thorell, Mikael Rydén, et al. Spatial mapping reveals human adipocyte subpopulations with distinct sensitivities to insulin. Cell metabolism, 33(9):1869–1882, 2021.

[18] David L Morris, Kae Won Cho, Jennifer L DelProposto, Kelsie E Oatmen, Lynn M Geletka, Gabriel Martinez-Santibanez, Kanakadurga Singer, and Carey N Lumeng. Adipose tissue macrophages function as antigen-presenting cells and regulate adipose tissue cd4+ t cells in mice. Diabetes, 62(8):2762–2772, 2013.

[19] Cara E Porsche, Jennifer B Delproposto, Lynn Geletka, Robert O'Rourke, and Carey N Lumeng. Obesity results in adipose tissue t cell exhaustion. JCI insight, 6(8), 2021.

[20] Patrik L Ståhl, Fredrik Salmén, Sanja Vickovic, Anna Lundmark, José Fernández Navarro, Jens Magnusson, Stefania Giacomello, Michaela Asp, Jakub O Westholm, Mikael Huss, et al. Visualization and analysis of gene expression in tissue sections by spatial transcriptomics. Science, 353(6294):78–82, 2016.

[21] Can Liu, Pinhao Li, Hui Li, Sicong Wang, Lifeng Ding, Hanbin Wang, Hui Ye, Yue Jin, Jinchao Hou, Xiangming Fang, et al. Trem2 regulates obesity-induced insulin resistance via adipose tissue remodeling in mice of high-fat feeding. Journal of Translational Medicine, 17(1):1–11, 2019.

[22] Omar Sharif, Julia Stefanie Brunner, Ana Korosec, Rui Martins, Alexander Jais, Berend Snijder, Andrea Vogel, Michael Caldera, Anastasiya Hladik, Karin Lakovits, et al. Beneficial metabolic effects of trem2 in obesity are uncoupled from its expression on macrophages. Diabetes, 70(9):2042–2057, 2021.

[23] Ada Weinstock, Emily J Brown, Michela L Garabedian, Stephanie Pena, Monika Sharma, Juan Lafaille, Kathryn J Moore, and Edward A Fisher. Single-cell rna sequencing of visceral adipose tissue leukocytes reveals that caloric restriction following obesity promotes the accumulation of a distinct macrophage population with features of phagocytic cells. Immunometabolism, 1, 2019.

[24] Tracey McLaughlin, Shelley E Ackerman, Lei Shen, Edgar Engleman, et al. Role of innate and adaptive immunity in obesity-associated metabolic disease. The Journal of clinical investigation, 127(1):5–13, 2017.

[25] Indika Rajapakse and Stephen Smale. Emergence of function from coordinated cells in a tissue. Proceedings of the National Academy of Sciences, 114(7):1462–1467, 2017.

[26] Jiyeon Yang, Lixiao Zhang, Caijia Yu, Xiao-Feng Yang, and Hong Wang. Monocyte and macrophage differentiation: circulation inflammatory monocyte as biomarker for inflammatory diseases. Biomarker research, 2(1):1–9, 2014.

[27] Brian F Zamarron, Taleen A Mergian, Kae Won Cho, Gabriel Martinez-Santibanez, Danny Luan, Kanakadurga Singer, Jennifer L DelProposto, Lynn M Geletka, Lindsey A Muir, and Carey N Lumeng. Macrophage proliferation sustains adipose tissue inflammation in formerly obese mice. Diabetes, 66(2):392–406, 2017.

[28] Takayoshi Suganami and Yoshihiro Ogawa. Adipose tissue macrophages: their role in adipose tissue remodeling. Journal of leukocyte biology, 88(1):33–39, 2010.

[29] Jia Xue, Susanne V Schmidt, Jil Sander, Astrid Draffehn, Wolfgang Krebs, Inga Quester, Dominic De Nardo, Trupti D Gohel, Martina Emde, Lisa Schmidleithner, et al. Transcriptome-based network analysis reveals a spectrum model of human macrophage activation. Immunity, 40(2):274–288, 2014.

[30] David A Hill, Hee-Woong Lim, Yong Hoon Kim, Wesley Y Ho, Yee Hoon Foong, Victoria L Nelson, Hoang CB Nguyen, Kavya Chegireddy, Jihoon Kim, Andreas Habertheuer, et al. Distinct macrophage populations direct inflammatory versus physiological changes in adipose tissue. Proceedings of the National Academy of Sciences, 115(22):E5096–E5105, 2018.

[31] Elizabeth A Rondini and James G Granneman. Single cell approaches to address adipose tissue stromal cell heterogeneity. Biochemical Journal, 477(3):583–600, 2020.

[32] Michiko Itoh, Hideaki Kato, Takayoshi Suganami, Kuniha Konuma, Yoshio Marumoto, Shuji Terai, Hiroshi Sakugawa, Sayaka Kanai, Miho Hamaguchi, Takahiro Fukaishi, et al. Hepatic crown-like structure: a unique histological feature in non-alcoholic steatohepatitis in mice and humans. PloS one, 8(12):e82163, 2013.

[33] Meiling Ren, Huanji Xu, Hongwei Xia, Qiulin Tang, and Feng Bi. Simultaneously targeting soat1 and cpt1a ameliorates hepatocellular carcinoma by disrupting lipid homeostasis. Cell death discovery, 7(1):1–15, 2021.

[34] Elena A Pudova, Anna V Kudryavtseva, Maria S Fedorova, Andrew R Zaretsky, Dmitry S Shcherbo, Elena N Lukyanova, Anatoly Y Popov, Asiya F Sadritdinova, Ivan S Abramov, Sergey L Kharitonov, et al. Hk3 overexpression associated with epithelial-mesenchymal transition in colorectal cancer. BMC genomics, 19(3):5–13, 2018.

[35] Andreea Barbu, Osama A Hamad, Lars Lind, Kristina N Ekdahl, and Bo Nilsson. The role of complement factor c3 in lipid metabolism. Molecular immunology, 67(1):101–107, 2015.

[36] Chun-Seok Cho, Jingyue Xi, Yichen Si, Sung-Rye Park, Jer-En Hsu, Myungjin Kim, Goo Jun, Hyun Min Kang, and Jun Hee Lee. Microscopic examination of spatial transcriptome using seq-scope. Cell, 2021.

[37] Shannon M Reilly and Alan R Saltiel. Adapting to obesity with adipose tissue inflammation. Nature Reviews Endocrinology, 13(11):633–643, 2017.

[38] Daniel A Winer, Shawn Winer, Lei Shen, Persis P Wadia, Jason Yantha, Geoffrey Paltser, Hubert Tsui, Ping Wu, Matthew G Davidson, Michael N Alonso, et al. B cells promote insulin resistance through modulation of t cells and production of pathogenic igg antibodies. Nature medicine, 17(5):610–617, 2011.

[39] Joseph F Cavallari, Emmanuel Denou, Kevin P Foley, Waliul I Khan, and Jonathan D Schertzer. Different th17 immunity in gut, liver, and adipose tissues during obesity: the role of diet, genetics, and microbes. Gut Microbes, 7(1):82–89, 2016.

[40] Nicole Jw De Wit, Hanneke Bosch-Vermeulen, Philip J de Groot, Guido JEJ Hooiveld, Mechteld M Grootte Bromhaar, Jenny Jansen, Michael Müller, and Roelof van der Meer. The role of the small intestine in the development of dietary fat-induced obesity and insulin resistance in c57bl/6j mice. BMC medical genomics, 1(1):1–16, 2008.

[41] Nicole JW De Wit, Mark V Boekschoten, Eva-Maria Bachmair, Guido JEJ Hooiveld, Philip J de Groot, Isabel Rubio-Aliaga, Hannelore Daniel, and Michael Müller. Dose-dependent effects of dietary fat on development of obesity in relation to intestinal differential gene expression in c57bl/6j mice. PLoS One, 6(4):e19145, 2011.

[42] Maeve Mullooly, Hannah P Yang, Roni T Falk, Sarah J Nyante, Renata Cora, Ruth M Pfeiffer, Derek C Radisky, Daniel W Visscher, Lynn C Hartmann, Jodi M Carter, et al. Relationship between crown-like structures and sex-steroid hormones in breast adipose tissue and serum among postmenopausal breast cancer patients. Breast Cancer Research, 19(1):1–10, 2017.

[43] Neil M Iyengar, Xi Kathy Zhou, Ayca Gucalp, Patrick G Morris, Louise R Howe, Dilip D Giri, Monica Morrow, Hanhan Wang, Michael Pollak, Lee W Jones, et al. Systemic correlates of white adipose tissue inflammation in early-stage breast cancer. Clinical Cancer Research, 22(9):2283–2289, 2016.

[44] Jodi M Carter, Tanya L Hoskin, M Alvaro Pena, Rushin Brahmbhatt, Stacey J Winham, Marlene H Frost, Melody Stallings-Mann, Derek C Radisky, Keith L Knutson, Daniel W Visscher, et al.

Macrophagic "crown-like structures" are associated with an increased risk of breast cancer in benign breast disease. Cancer Prevention Research, 11(2):113–119, 2018.

[45] Tulay Koru-Sengul, Ana M Santander, Feng Miao, Lidia G Sanchez, Merce Jorda, Stefan Glück, Tan A Ince, Mehrad Nadji, Zhibin Chen, Manuel L Penichet, et al. Breast cancers from black women exhibit higher numbers of immunosuppressive macrophages with proliferative activity and of crown-like structures associated with lower survival compared to non-black latinas and caucasians. Breast cancer research and treatment, 158(1):113–126, 2016.

[46] Eugenia E Calle, Carmen Rodriguez, Kimberly Walker-Thurmond, and Michael J Thun. Overweight, obesity, and mortality from cancer in a prospectively studied cohort of us adults. New England Journal of Medicine, 348(17):1625–1638, 2003.

[47] Emily Jane Gallagher and Derek LeRoith. Obesity and diabetes: the increased risk of cancer and cancer-related mortality. Physiological reviews, 95(3):727–748, 2015.

[48] Payal Tiwari, Ariane Blank, Chang Cui, Kelly Q Schoenfelt, Guolin Zhou, Yanfei Xu, Galina Khramtsova, Funmi Olopade, Ajay M Shah, Seema A Khan, et al. Metabolically activated adipose tissue macrophages link obesity to triple-negative breast cancer. Journal of Experimental Medicine, 216(6):1345–1358, 2019.

[49] Susanne C van den Brink, Anna Alemany, Vincent van Batenburg, Naomi Moris, Marloes Blotenburg, Judith Vivié, Peter Baillie-Johnson, Jennifer Nichols, Katharina F Sonnen, Alfonso Martinez Arias, et al. Single-cell and spatial transcriptomics reveal somitogenesis in gastruloids. Nature, 582(7812):405–409, 2020.

[50] Xinxin Zhang, Yujia Lan, Jinyuan Xu, Fei Quan, Erjie Zhao, Chunyu Deng, Tao Luo, Liwen Xu, Gaoming Liao, Min Yan, et al. Cellmarker: a manually curated resource of cell markers in human and mouse. Nucleic acids research, 47(D1):D721–D728, 2019.

[51] Tracy SP Heng, Michio W Painter, Kutlu Elpek, Veronika Lukacs-Kornek, Nora Mauermann, Shannon J Turley, Daphne Koller, Francis S Kim, Amy J Wagers, Natasha Asinovski, et al. The immunological genome project: networks of gene expression in immune cells. Nature immunology, 9(10):1091–1094, 2008.

[52] Gerard Salton and Christopher Buckley. Term-weighting approaches in automatic text retrieval. Information processing & management, 24(5):513–523, 1988.

[53] Erick Armingol, Adam Officer, Olivier Harismendy, and Nathan E Lewis. Deciphering cell–cell interactions and communication from gene expression. Nature Reviews Genetics, 22(2):71–88, 2021.

[54] Matan Gavish and David L Donoho. The optimal hard threshold for singular values is $4/\sqrt{3}$. IEEE Transactions on Information Theory, 60(8):5040 – 5053, 2014.

[55] AM Turing. The chemical basis of morphogenesis. Philos. Trans. Roy. Soc., 1952.

[56] Philip K Maini. Turing's mathematical theory of morphogenesis. 2012.

[57] Leon O Chua. Local activity is the origin of complexity. International journal of bifurcation and chaos, 15(11):3435–3456, 2005.

5 Supplementary Materials

Algorithm 1: Clustering and Visualization

Input: Data matrix $\mathbf{X}_{m\times n} = (\mathbf{x}_1, ..., \mathbf{x}_n) \in \mathbb{R}^{m\times n}$ where m rows are genes and n columns are cells.

Output: Cell clusters and a low dimensional projection

1. Compute the sample mean μ_n and the centered matrix $\mathbf{X}_c = \mathbf{X} - \mu_n \mathbf{1}^\top$ where $\mathbf{1}$ is a vector of ones
2. Compute the SVD of $\mathbf{X}_c = \mathbf{U}\mathbf{\Sigma}\mathbf{V}^\top$
3. Construct $\mathbf{P}_{n\times r} = \begin{bmatrix} v_1 & v_2 & \dots & v_r \end{bmatrix}$ where each column in $\mathbf{P}$ is a right singular vector of $\mathbf{X}_c$. Here r can be chosen using the optimal hard threshold [54] on $\mathbf{X}_c$
4. Construct a similarity matrix $\mathbf{A}_{n\times n}$ from $\mathbf{P}$ by determining the distance between each row. The choice of distance measure depends on the data type and user preference. Examples include Gaussian similarity, Euclidean distance, Manhattan distance (city block distance), Kullbeck-Liebler divergence, and correlation
5. Perform clustering: spectral or modularity clustering on $\mathbf{A}$ with k clusters. k can be chosen using domain knowledge or by testing multiple values of k and evaluating the best performance. Note: k may be $\leq r$
6. Visualization: t-SNE or UMAP to reduce the dimensions of $\mathbf{P}$ and visualize data colored according to clusters

Algorithm 2: Cell Type Localization and Spot Deconvolution

Input: scRNA-seq feature-barcode matrices $\mathbf{F}_{(s)} \in \mathbb{R}^{m\times n}$ where m rows are genes and n columns are cells; ST feature-barcode matrices $\mathbf{T}_{(s)} \in \mathbb{R}^{m\times n}$ where m rows are genes and n columns are tissue spots

Output: Tissue spot cell type assignments

1. Perform spectral clustering on $\mathbf{F}_{(s)}$ aggregated across all timepoints s
2. Rank m genes for each cell type (cluster) k. Genes are ranked by ubiquity, cluster-averaged expression, and uniqueness (see Methods and Materials)
3. Construct cell type-specific signatures $\mathbf{S}_{(k)} \in \mathbb{R}^{50\times 1}$, containing highly ranked genes common across timepoints
4. Query expression of cell type-specific signature genes at tissue spots by finding $\mathbf{T}_{(s)} \subset \mathbf{S}_{(k)}$
5. Assign to each tissue spot the cell type expressing the most and at minimum 5 of its signature genes
6. Deconvolute tissue spots: repeat step 5 until an attempt to assign each cell type to every tissue spot has been made. Each successive assignment represents a deconvoluted tissue layer.

Algorithm 3: Ligand-Receptor Colocalization Dynamics

Input: Table of ligand-receptor pairs $\mathbf{L}$, from literature

Output: Global state matrix, $\mathbf{S} \in \mathbb{R}^{n \times n}$

1 **ST Data:** For each ligand-receptor pair p in $\mathbf{L}$, assign colocalization score:

$$c = \begin{cases} 1 & \text{if } l > 0 \text{ and } r > 0 \\ 0 & \text{otherwise} \end{cases},$$

where l and r are UMI counts for the ligand and receptor in p, respectively, at a given tissue spot

2 **scRNA-seq Data:** If p has a colocalization score of 1 at least once across the tissue, construct contingency table $\mathbf{C}_{2\times n}$, where $\mathbf{C_{11}}$ and $\mathbf{C_{21}}$ are the proportions of single cells classified as 'cell type 1' with l and $r > 3$, respectively, $\mathbf{C_{12}}$ and $\mathbf{C_{22}}$ are the proportions of single cells classified as 'cell type 2' with l and $r > 3$, respectively, and so on up to 'cell type n' ($\mathbf{C_{1n}}$ and $\mathbf{C_{2n}}$)

3 Construct local state matrix for $\mathbf{S}_{(p)} \in \mathbb{R}^{n \times n}$, by finding the mean between all pairwise combinations of ligand-specific ($\mathbf{C_{11}}$,$\mathbf{C_{12}}$,...,$\mathbf{C_{1n}}$) and receptor-specific ($\mathbf{C_{21}}$,$\mathbf{C_{22}}$,...,$\mathbf{C_{2n}}$) proportions in $\mathbf{C}$

4 After performing steps 1-3 for all p in $\mathbf{L}$, define global state matrix, $\mathbf{S} \in \mathbb{R}^{n \times n}$, by computing the element-wise mean across all $\mathbf{S}_{(p)} \in \mathbb{R}^{n \times n} : \sum_{p=1}^{m} \mathbf{S}_{(p)}/m$, where m is the number of ligand-receptor pairs, p

6 Supplementary Notes

6.1 Turing's Model of Pattern Formation

Alan Turing's contribution to mathematical biology produced remarkable insights into the formation of patterns, for example animal stripes and spots or limb development [55]. Turing described the state of a biological system in terms of the concentrations and "diffusibilities" of its substances – referred to as "morphogens." The mathematical formulation of Turing's model for morphogenesis relies on a set of differential equations – reaction-diffusion equations [56].

Turing postulated that discontinuous diffusion drives a system to become unstable and establish spatial patterns due to a breakdown in symmetry and homogeneity. Turing's two-cell system contains variables $\mathbf{x}_1, \mathbf{y}_1$ representing concentrations of molecules (or proteins) for the first cell and $\mathbf{x}_2, \mathbf{y}_2$ for the second cell:

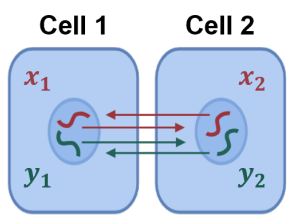

Turing's two-cell reaction-diffusion equations are given as:

$$\begin{aligned} \dot{\mathbf{x}}_1 &= (5\mathbf{x}_1 - 6\mathbf{y}_1 + 1) + 0.5\,(\mathbf{x}_2 - \mathbf{x}_1) \\ \dot{\mathbf{y}}_1 &= (6\mathbf{x}_1 - 7\mathbf{y}_1 + 1) + 4.5\,(\mathbf{y}_2 - \mathbf{y}_1) \\ \dot{\mathbf{x}}_2 &= (5\mathbf{x}_2 - 6\mathbf{y}_2 + 1) + 0.5\,(\mathbf{x}_1 - \mathbf{x}_2) \\ \dot{\mathbf{y}}_2 &= \underbrace{(6\mathbf{x}_2 - 7\mathbf{y}_2 + 1)}_{\substack{\textbf{Reaction (A)} \\ \text{(within-cell)}}} + \underbrace{4.5\,(\mathbf{y}_1 - \mathbf{y}_2)}_{\substack{\textbf{Diffusion } (-\mathbf{L}) \\ \text{(between-cell)}}} \end{aligned} \tag{1}$$

where, $\dot{\mathbf{x}} = \frac{d\mathbf{x}}{dt}, \dot{\mathbf{y}} = \frac{d\mathbf{y}}{dt}$ and $\mathbf{x}, \mathbf{y} > 0$. We can rewrite Equation 1 as follows:

$$\begin{pmatrix} \dot{\mathbf{x}}_1 \\ \dot{\mathbf{y}}_1 \\ \dot{\mathbf{x}}_2 \\ \dot{\mathbf{y}}_2 \end{pmatrix} = \begin{pmatrix} 5 & -6 & 0 & 0 \\ 6 & -7 & 0 & 0 \\ 0 & 0 & 5 & -6 \\ 0 & 0 & 6 & -7 \end{pmatrix} \begin{pmatrix} \mathbf{x}_1 \\ \mathbf{y}_1 \\ \mathbf{x}_2 \\ \mathbf{y}_2 \end{pmatrix} + \begin{pmatrix} -0.5 & 0 & 0.5 & 0 \\ 0 & -4.5 & 0 & 4.5 \\ 0.5 & 0 & -0.5 & 0 \\ 0 & 4.5 & 0 & -4.5 \end{pmatrix} \begin{pmatrix} \mathbf{x}_1 \\ \mathbf{y}_1 \\ \mathbf{x}_2 \\ \mathbf{y}_2 \end{pmatrix} \tag{2}$$

$$= \begin{pmatrix} 4.5 & -6 & 0.5 & 0 \\ 6 & -11.5 & 0 & 4.5 \\ 0.5 & 0 & 4.5 & -6 \\ 0 & 4.5 & 6 & -11.5 \end{pmatrix} \begin{pmatrix} \mathbf{x}_1 \\ \mathbf{y}_1 \\ \mathbf{x}_2 \\ \mathbf{y}_2 \end{pmatrix} \tag{3}$$

Separately, the reaction and diffusion dynamics of the system are stabilizing (Equation 2), as their eigenvalues are negative ($\lambda_i(\mathbf{A}) = -1, i = 1, 2, 3, 4$ and $\lambda_i(-\mathbf{L}) = -9, -1, 0, 0, i = 1, 2, 3, 4$, respectively). The combined system has one positive and three negative eigenvalues ($\lambda_i = 1, 1, 14, i = 1, 2, 3, 4$), rendering the system unstable (Equation 3). Turing's beautifully designed two-cell system demonstrated that only with diffusion is the system unstable – an instability needed for the formation of pattern [25, 57]. We can mathematically represent this system in the form $\frac{d\mathbf{x}}{dt} = \mathbf{A}\mathbf{x} - \mathbf{L}\mathbf{x}, \mathbf{x} = (\mathbf{x}_1, ..., \mathbf{x}_n)$.

Here, Turing-based representation of our spatial and single cell transcriptomics data captures adipose tissue instability underlying emerging insulin resistance at the onset of obesity.

7 Supplementary Figures and Tables

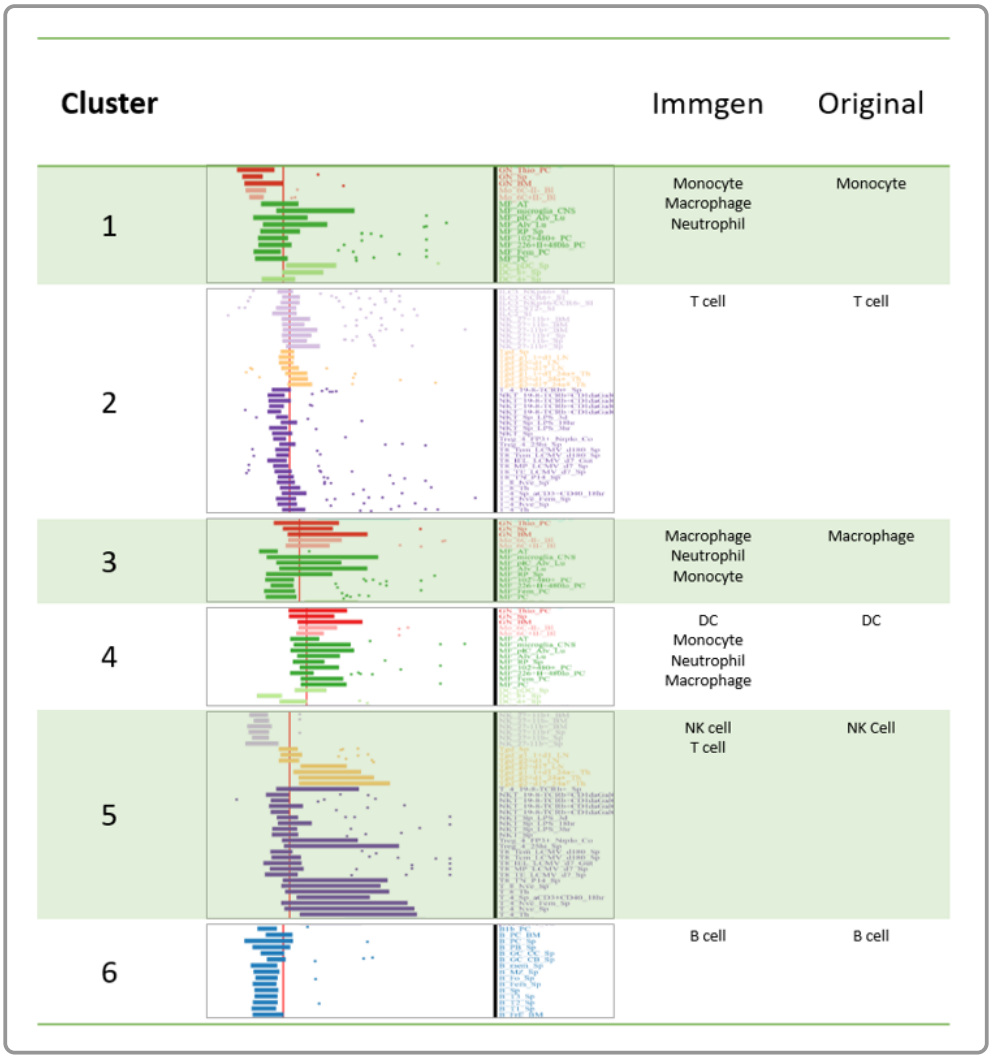

Figure S1: **Validation of clustering and cell type annotation.** Cell types in the single-cell data align with Immgen signatures.

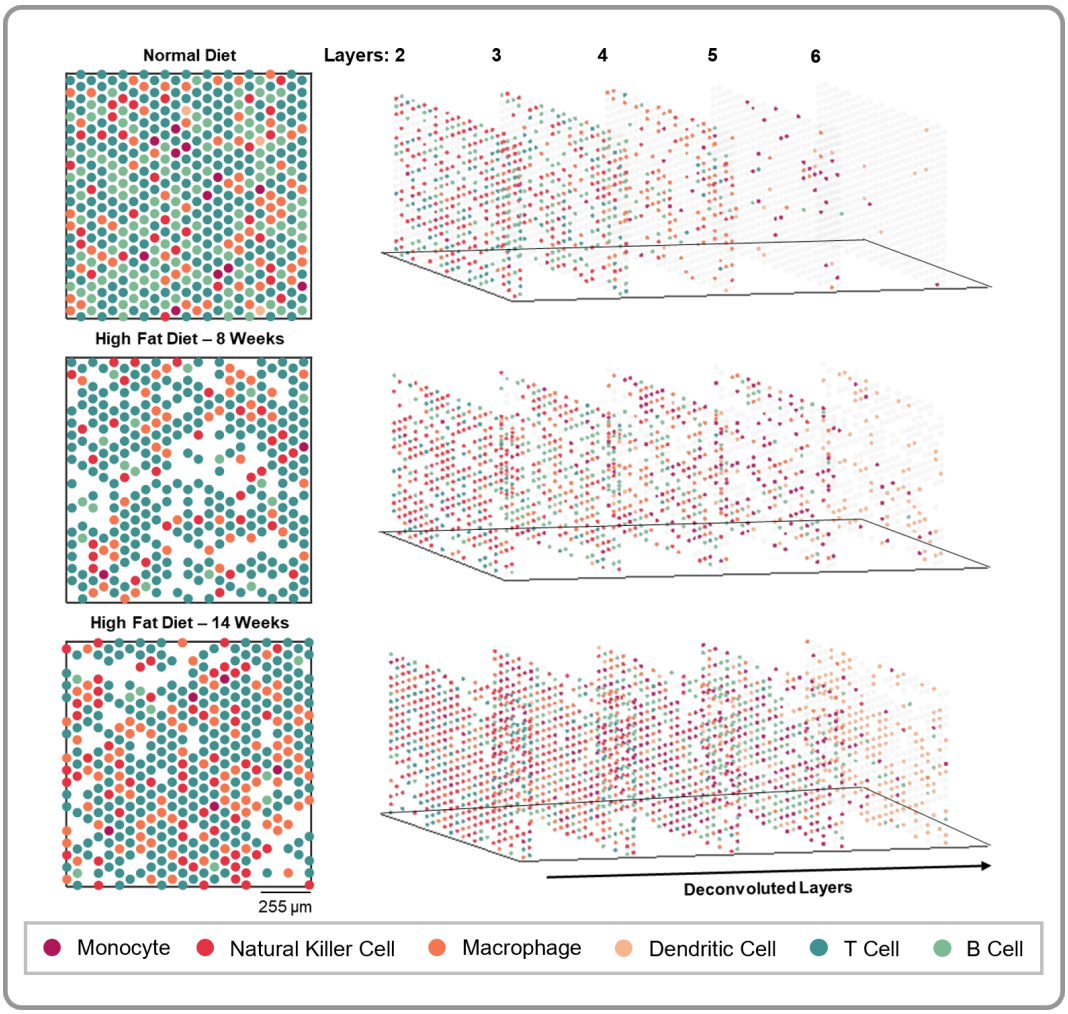

Figure S2: **Deconvoluted tissue assignment layers.** Annotated spatial transcriptomics tissue landscapes over time, zoomed in for clearer view of cell type composition and distribution. Cell type assignments in the left panels represent the dominant spot assignments after performing spot deconvolution (i.e. Layer 1). (Rightmost panels) Non-dominant deconvoluted layers (Layers 2 - 6) of tissue spot assignments for zoomed in region. Light gray spots represent spots that were unassigned because no remaining cell types met the gene expression threshold.

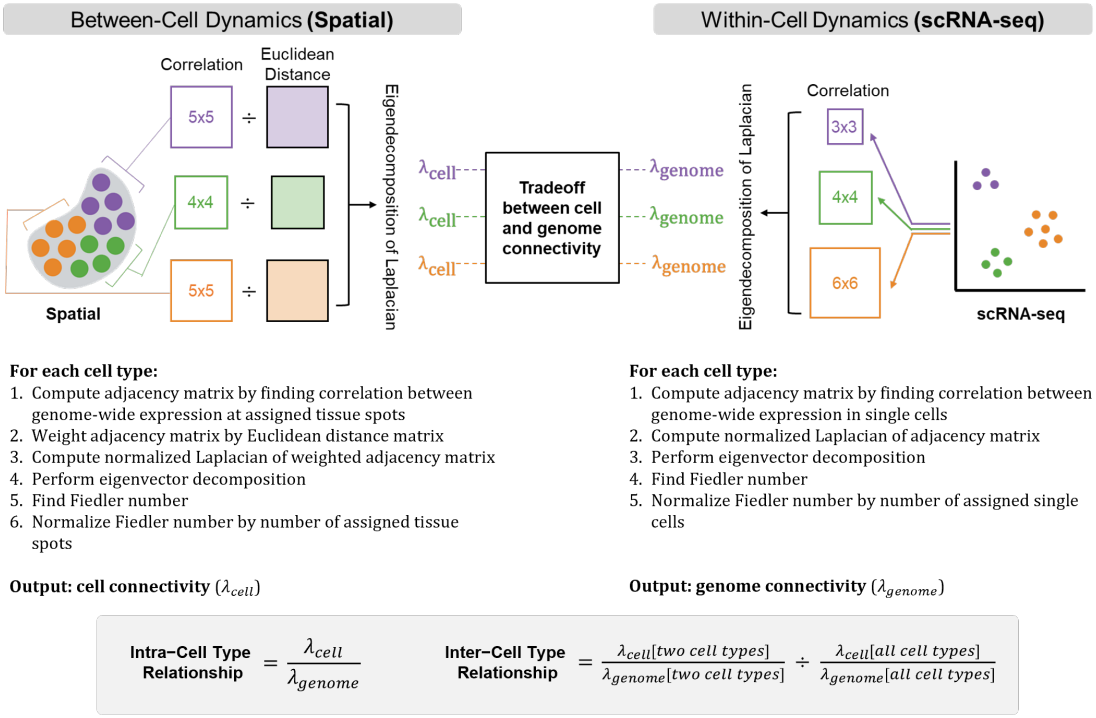

Figure S3: **Overview of Turing-inspired model for describing adult adipose tissue dynamics.**

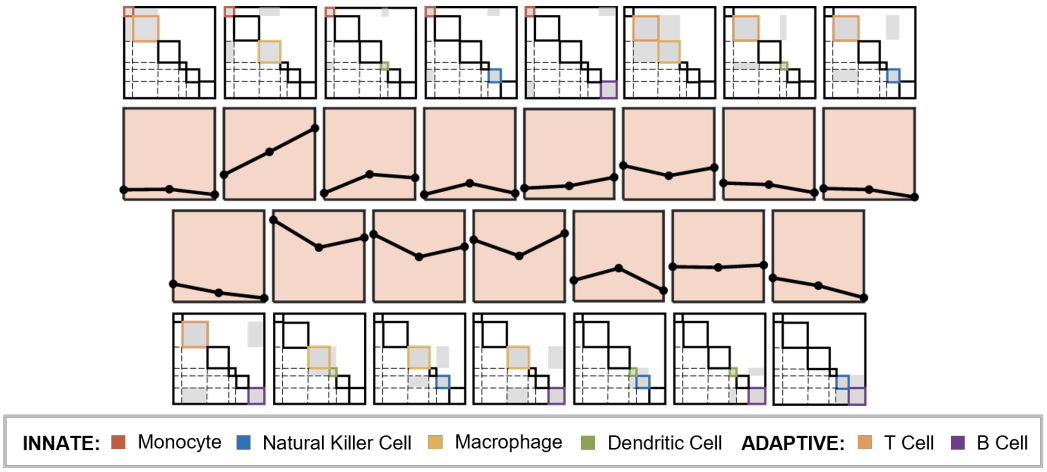

Figure S4: **Inter-cell type contribution to multicellular tissue function for all pairs of immune cell types.**

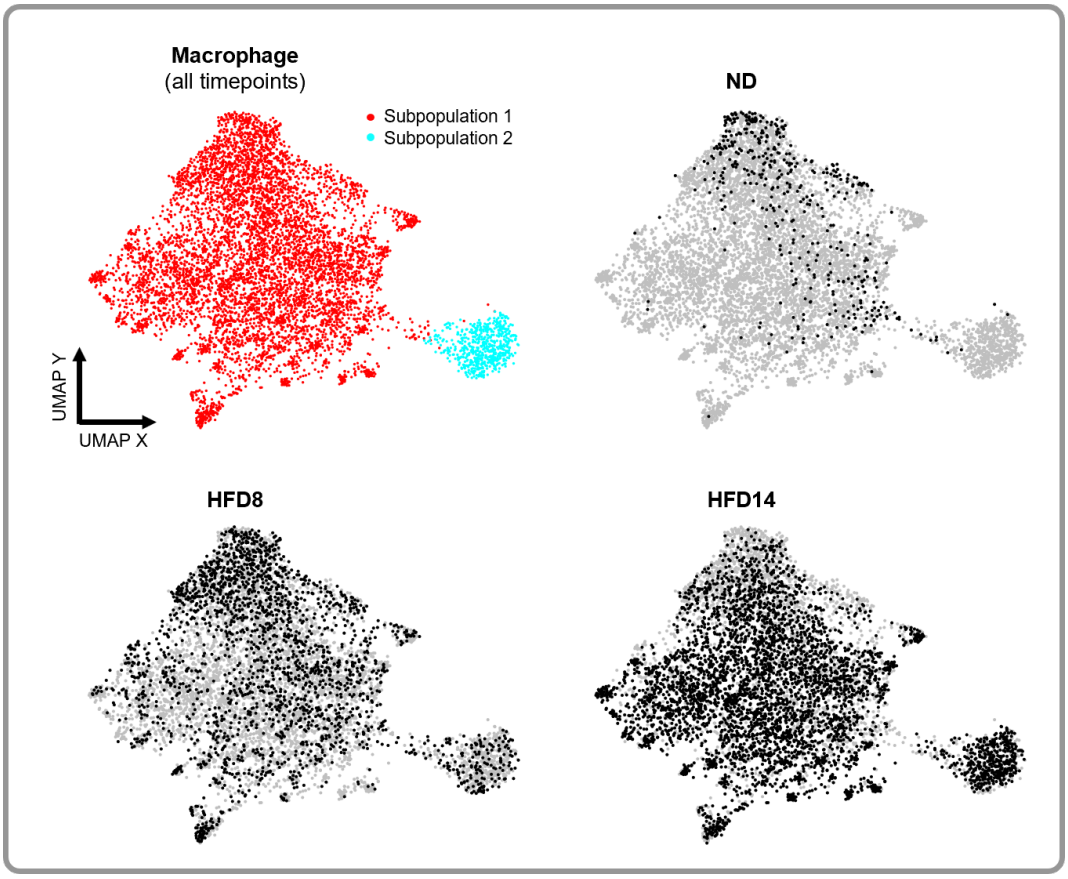

Figure S5: **Spectral clustering on single cells assigned macrophage.** Subpopulation 2 is significantly enriched for *Cd9*.

Monocyte	T Cell	Macrophage	Dendritic Cell	Natural Killer Cell	B Cell
Gngt2	*Il7r*	*C1qb*	*Ppt1*	*Ccl5*	*Igkc*
Msrb1	*Thy1*	*C1qa*	*Cd24a*	*AW112010*	*Cd79b*
Clec4a3	*H2-Q7*	*C1qc*	*Naaa*	*Ugcg*	*H2-DMb2*
Clec4a1	*Ets1*	*Mrc1*	*Batf3*	*H2-Q7*	*Ebf1*
Csf1r	*Ptprcap*	*Csf1r*	*Psmb9*	*Ptprcap*	*Ighm*
Gsr	*Ltb*	*Dab2*	*Naga*	*Ctla2a*	*Plac8*
Plac8	*Malat1*	*Trem2*	*Wdfy4*	*Klrk1*	*H2-Eb1*
Cebpb	*Tmsb4x*	*Pf4*	*Fnbp1*	*Gimap6*	*Mef2c*
Rnf149	*Rac2*	*Adgre1*	*BC028528*	*H2-Q6*	*H2-Aa*
Cybb	*Gata3*	*C3ar1*	*Irf8*	*Gimap5*	*H2-Ab1*
Mafb	*Gimap6*	*C5ar1*	*Cbfa2t3*	*Ets1*	*Cd74*
Cd300a	*Tpt1*	*Fcgr3*	*Ppm1m*	*Tyrobp*	*Cd83*
Fcgr3	*Eef1a1*	*Lilr4b*	*Rgs10*	*Fcer1g*	*Serp1*
Emilin2	*Fau*	*Ehd4*	*Aif1*	*Id2*	*Cd37*
Ms4a6c	*Actb*	*Pltp*	*Rnase6*	*Rac2*	*Gimap6*
Tpd52	*H2-K1*	*Slc11a1*	*Xcr1*	*Cd52*	*Pou2f2*
Pla2g7	*Cd52*	*Glul*	*Id2*	*Ctsd*	*Ly6e*
Ncf2	*H2-D1*	*Cd84*	*Psme1*	*Malat1*	*Foxp1*
Lyz2	*Tmsb10*	*Lgmn*	*Lsp1*	*Tmsb4x*	*Ralgps2*
S100a4	*Ubb*	*Slc6a6*	*Syngr2*	*Lgals1*	*Ly6a*
Prdx5	*Actg1*	*Mafb*	*H2-DMb1*	*Ptprc*	*Trp53inp1*
Ifitm3	*Coro1a*	*Abhd12*	*Plbd1*	*Actb*	*Fam214a*
Ccl6	*B2m*	*Ccl9*	*Anpep*	*Arhgdib*	*Ptprcap*
Alox5ap	*Pfn1*	*Cybb*	*H2-Aa*	*Eef1a1*	*Fam46c*
Ccl9	*Hspa8*	*Apoe*	*Tap1*	*Tpt1*	*Ets1*
Sirpa	*Eif1*	*Daglb*	*H2-Eb1*	*Tmsb10*	*Shisa5*
Apoe	*Ppia*	*Cd14*	*Rtl8b*	*H2-K1*	*Scd1*
Hck	*H2-Q6*	*Lipa*	*Unc119*	*Fau*	*D10Wsu102e*
Plbd1	*S100a4*	*Cd36*	*Rab7b*	*H2-D1*	*Malat1*
Tgfbi	*Fth1*	*Mt1*	*Cadm1*	*Actg1*	*Capg*
Pou2f2	*Rack1*	*Lyz2*	*Rab32*	*Coro1a*	*Phgdh*
Zeb2	*H3f3b*	*Pld3*	*H2afz*	*Pfn1*	*Dennd4a*
Cxcr4	*Uba52*	*Tbxas1*	*Rtl8a*	*Dok2*	*Srgn*
Lilr4b	*Srgn*	*Ctsd*	*Atpif1*	*B2m*	*Cacna1e*
Metrnl	*Ptprc*	*Sirpa*	*H2-Ab1*	*Ppia*	*Tmsb4x*
Lgals3	*Eef2*	*Tmem106a*	*Sh3bp1*	*Ubb*	*Cd52*
Ifi27l2a	*Sh3bgrl3*	*Sdc3*	*Mpeg1*	*Cfl1*	*Tpt1*
Tyrobp	*Cfl1*	*Blvrb*	*Olfm1*	*Myl6*	*Fau*
Mpeg1	*Ftl1*	*Cd63*	*Kctd12*	*Sh3bgrl3*	*Eef1a1*
Plin2	*Hsp90ab1*	*Timp2*	*Plekho1*	*Eif1*	*Tnfrsf13b*
Fcer1g	*Ptma*	*Atp6v1b2*	*Actr3*	*Cd37*	*Unc93b1*
Srgn	*Ccnd2*	*Selenop*	*Atox1*	*Ccnd2*	*Man1a*
Ctss	*Gm10076*	*Lpl*	*Cd74*	*Laptm5*	*St6gal1*
Nfe2l2	*Myl6*	*Dhrs3*	*Psme2*	*H3f3b*	*Actb*
Wfdc17	*Ddx5*	*Ccl6*	*Gltp*	*Uba52*	*Pkig*
Cd68	*Laptm5*	*Zeb2*	*Psmb8*	*Ikzf3*	*Fth1*
Lamp1	*Junb*	*H2-Aa*	*Lyz2*	*Anxa2*	*Ikzf3*
Lyn	*Oaz1*	*Capg*	*Ckb*	*Bcl2*	*H3f3b*
Taldo1	*Jund*	*Ctsl*	*Pomp*	*Lcp1*	*Eif1*
Sat1	*S100a10*	*H2-Eb1*	*Alox5ap*	*Rack1*	*Ctss*

Table S1: Cell-type signatures. 50 highest scoring genes per cell type.

Ligand	Receptor	CLS (%)*	Control (%)*	Ligand Cell Type	Receptor Cell Type
Apoe	*Lrp1*	0.0	20.6	ATM	Monocyte
		66.7	20.5	Monocyte	ATM
		81.8	28.6	ATM	ATM
App	*Gpc1*	0.0	4.4	Monocyte	NKC
		5.1	4.8	ATM	NKC
		25.6	5.7	ATM	NKC
Calr	*Itgav*	0.0	0.0	ATDC	NKC
		28.2	12.2	ATDC	ATM
		50.4	8.6	ATM	ATM
Col4a1	*Cd93*	0.0	1.9	ATM	ATM
		25.6	9.2	Monocyte	ATM
		43.8	11.4	ATM	ATM
Gnai2	*F2r*	0.0	0.6	ATDC	NKC
		28.2	9.6	ATDC	T Cell
		65.3	22.9	ATDC	NKC
Hsp90b1	*Lrp1*	0.0	1.9	ATDC	Monocyte
		12.8	10.0	ATDC	ATM
		37.2	17.1	ATM	ATM
Lgals3	*Lgals3bp*	0.0	1.9	ATDC	Monocyte
		30.8	26.2	ATDC	ATM
		57.0	40.0	Monocyte	ATM
Lpl	*Sdc1*	0.0	1.3	ATM	B Cell
		59.0	33.2	ATM	ATM
		93.4	42.9	ATM	ATM
Mif	*Cd74*	0.0	0.0	B Cell	ATDC
		2.6	2.2	ATM	ATDC
		35.5	0.0	ATM	ATDC
Nid1	*Itgb1*	0.0	5.0	B Cell	ATDC
		10.3	11.8	B Cell	ATDC
		27.3	5.7	B Cell	ATM
Thbs1	*Cd36*	0.0	12.5	Monocyte	ATDC
		17.9	15.3	Monocyte	ATM
		25.6	2.9	Monocyte	ATM
Timp2	*Itgb1*	0.0	2.5	ATM	ATDC
		48.7	17.0	ATM	ATDC
		61.2	17.1	ATM	ATM

Table S2: **Summary of ligand-receptor activity at CLS Neighborhoods.** LR pairs whose colocalization at CLS neighborhoods preferentially increased over time from no colocalization in ND (white rows) to increased colocalization at 8w (light grey rows) and 14w (dark grey rows) are shown. * = percent of neighborhood colocalized.